8-2019

Investigation of Graphene Interconnections for Multifunctional Reconfigurable Antenna Beam Steering

Joshua R. Perkins
Utah State University

INVESTIGATION OF GRAPHENE INTERCONNECTIONS FOR MULTIFUNCTIONAL RECONFIGURABLE ANTENNA BEAM STEERING

by

Joshua R. Perkins

A thesis submitted in partial fulfillment
of the requirements for the degree

of

MASTER OF SCIENCE

in

Electrical Engineering

Approved:

Bedri Cetiner, Ph.D. Major Professor	T.-C. Shen, Ph.D. Committee Member
Doran Baker, Ph.D. Committee Member	Richard S. Inouye, Ph.D. Vice Provost for Graduate Studies

UTAH STATE UNIVERSITY
Logan, Utah

2019

ABSTRACT

INVESTIGATION of GRAPHENE INTERCONNECTIONS FOR MULTIFUNCTIONAL RECONFIGURABLE ANTENNA BEAM STEERING

by

Joshua R. Perkins, Master of Science

Utah State University, 2019

Major Professor: Bedri Cetiner, Ph.D.
Department: Electrical and Computer Engineering

A multi-functional re-configurable antenna (MRA) using graphene nanoelectromechanical system (NEMS) switches and tantalum nitride (TaN) bias lines is designed and investigated by full-wave electromagnetic (EM) analyses. The MRA is based on a reconfigurable parasitic layer concept. The parasitic surface layer geometry of is modified, by controlling interconnecting graphene-based NEMS switches, thus resulting in beam-steering capability. The NEMS switches are controlled by dc signals applied to TaN bias lines. The TaN bias lines are highly RF resistive thin films of which impact on the MRA performance is also investigated by full-wave EM analyses. These investigations yielded two main results, which can be used to develop graphene switch based MRAs in the near future: 1) Graphene switches can be used to control the surface geometry of parasitic layer, and thus the electrical and mechanical advantages provided by graphene switches can be exploited. 2) Any deleterious mutual coupling can be avoided by using TaN based high resistive control lines that do not interfere with the radiating part of the MRA.

(71 pages)

PUBLIC ABSTRACT

INVESTIGATION of GRAPHENE INTERCONNECTIONS FOR MULTIFUNCTIONAL RECONFIGURABLE ANTENNA
BEAM STEERING
Joshua R. Perkins

In high frequency, high-performance wireless communications, direct line of sight antennas are common. The issue with the line of sight antennas is the need to redirect the physical antenna to achieve the best possible reception. Classical redirections are done by mechanical movements: hand tuning and motors. Our multi-functional re-configurable antenna (MRA) concept allows for electrical and non-mechanical antenna reorientation. This work investigates two important concepts in the development and enhancement of future MRA devices: special, non-interfering, control signal circuitry and nano-sized switching devices that are controlled by the special circuitry. The investigation was conducted with the use of commercially available antenna modeling software: ANSYS High Frequency System Solver.

This thesis is dedicated to Mahirah binti Zaini, Ben Zeller, my parents, and siblings for their overwhelming support of my ambitions.

Mahirah, you have been a constant source of encouragement and strength through both my undergraduate degree and my graduate research. This grand educational adventure has brought us closer together and taught us many lessons. I have loved and cherished every moment with you.

Ben Zeller, you have been an incredible friend and colleague throughout the years. I look forward to completing more projects with you in the future.

My parents, my brother Kyle, and my sister Elaina thank you for always challenging me and supporting me where they can.

ACKNOWLEDGMENTS

I must extend my gratitude to my advisors. Thank you. Dr. T.-C. Shen, for taking the time to provide mentorship and guidance. If I had not met and worked with you, I might not have made it this far. I look forward to any collaborations we can do in the future.

Thank you, Dr. Bedri Cetiner, for your support of my master's research and my pursuit of nanotechnology/nanofabrication through the last couple of years. I was able to learn from you, and you gave me space to grow.

Thank you, Merry Lu Zeller, for the time you took to edit and help me perfect my thesis.

Josh R. Perkins

CONTENTS

LIST OF TABLES

LIST OF FIGURES

CHAPTER 1

INTRODUCTION

In antenna design and wireless communications it is desired to have a high gain antenna able to transmit information across vast distances. Another desired trait in antenna design is having an omnidirectional radiation pattern to send and receive signals from all directions. These two desired properties are often trade-offs. High gain antennas suffer from high directivity and omnidirectional antennas suffer from low gain. Various methods have been established to overcome these trade-offs such as mechanical movements, phased array antennas, and MRAs.

MRA designs are very attractive as they can be applied to every standard antenna design. A desirable property in high frequency MRA design is achieving high gain in specified directions. A method of accomplishing this is beam steering by MRA elements [2]. Multifunctional reconfigurable antenna elements are implemented by use of devices such as electromechanical switches, and solid-state switches. Current electromechanical switches are advantageous over solid state switches in that they have less insertion loss, excellent isolation, and can operate from dc to any frequency [3]. The relative size of the electromechanical switch the device suffers from reduced switching speed and less durability than that of its solid-state counterparts.

The switching speed of electromechanical switches are determined by their physical size and material properties [4]. Graphene is one material that has excellent properties such as electron mobility, tensile strength, and high value of Young's modulus and can be used at the nanometer scale [5].

A graphene-based NEMs device is conceptualized based upon a study performed by P. Sharma *et al.* [6]. This device suffered from stiction to the lower electrodes, leading to the gradual decay and failure of the graphene switching element. In an MRA parasitic layer, it is not necessary to fully contact the lower switch electrode. It is of interest to fabricate the

graphene NEMS device onto the MRA parasitic surface. Before the graphene-based switching devices can be designed and fabricated would be imperative first to develop a graphene compatible MRA parasitic surface. Initial steps in this process are first, investigating classic parasitic MRA design, then adding the presence of DC control lines for individual graphene NEMS switch controls.

The DC control lines have an effect on the overall antenna system. The impact of the control lines depends on the resistive nature of the material used. Classically copper bias lines are used in MRA parasitic layer. However, a promising replacement, for copper, is tantalum nitride (TaN). TaN has shown high resistivity which is a desirable trait in metals that have little to no impact on the MRA design [7–9].

The following are the key contributions of the work presented in this thesis:

- This research provides an MRA antenna structure suitable for the study of Graphene NEMS switches.
- Chapter 3 & 4 show the design of an MRA with quartz glass in two separate configurations for the future development of higher frequency MRA designs.
- Chapter 5 explores the use of TaN dc bias lines.
- Chapter 6 Shows the design of co-planar wave guide (CPW) structure needed for the characterization of graphene NEMs switches.
- Chapter 7 provides the method of fabrication for the designs discussed in chapter 3 & 4.
- Chapter 8 briefly discusses the conceptual NEMS structure and additional suggestions for the fabrication of graphene-based NEMs devices.

CHAPTER 2

Literature Review

Currently our MRAs, use a form of solid state switching devices (PIN diodes) which could be replaced by either a MOSFET or a NEMS device [2]. The possibility of replacing the solid-state device with a NEMS device is interesting for several reasons; including, low insertion loss, high linearity, and higher isolation when compared to that of FET or PIN devices [3].

A simple NEMS device can be made by forming a membrane over conductive pad at the bottom of a trench. A previous study on this geometry by S.M. Kim et al. gives an interesting basis for the proposed study [4] however the geometry used in Ref. 4 fails to isolate the actuation, dc voltage from the signal path. One method of overcoming this is presented by P. Sharama et al. [10] where a dielectric layer is used to isolate the dc bias voltage from the RF signal path [11]. Another variation that can separate the signal from dc voltage is a three level electrode placement. In this scheme the RF signal line is placed atop of either a dielectric layer or pillar with a dc contact set in a trench bellow. Using variations such as these will allow for a mechanical switching device that can isolate the RF signal from the dc voltages.

Microelectromechanical switches (MEMS) suffer from longer switching times than that of solid-state switches [3]. One way to reduce the switching time is to decrease the size of the MEMS device. When decreasing the size of the MEMS device the conventional materials used becomes fragile at the nanometer scale [10]. Many alternatives to traditional metals have been studied. One material tested was graphene.

The positive properties that make graphene viable is a high value of Young's modulus and high tensile strength when compared to those of steel [5]. Graphene also as a natural nanometer scale material allows for both lower actuation voltage and higher switching speed than those of traditional metals. Usage of graphene will also allow for monolithic

integration in the development of our MRAs.

Additionally, it is desirable to use TaN bias lines with the graphene NEMS switches, because TaN has been shown to have tunable-resistivity.And as such, can be a conductive and have a highly resistive bias line [7, 8]. If placed on the parasitic surface the resistive bias line will have little to no impact on the performance of an MRA device.

CHAPTER 3

Antenna Design

An antenna must first be designed To study the effect of graphene and TaN on parasitic surfaces. One antenna geometry that is highly scaleable and compatible with the microfabrication process is a microstrip patch antenna. The design of a patch antenna involves the consideration of substrate material, substrate thickness, feeding methods, and fabrication processes.

A printed transparency film was selected as a photomask in the lithography process, this will limit the smallest dimension to 100 μm [12]. The transparency mask was also chosen because it is cheaper and suitable for this project. The photomask chosen could achieve smaller dimensions, a dimension limit of 500 μm is a safe range for this design.

3.1 Patch Antenna Design

Three variables in designing a patch antenna is; the desired resonant frequency, best substrate for the design and its electronic properties. Since this design will be used to study both graphene and tantalum nitride it is necessary to select an RF compatible substrate that has little loss up to 100 GHz with a low dielectric constant. The substrate chosen must also be compatible with graphene synthesis.

3.1.1 Resonant Frequency

A patch with a resonant frequency in the 8-11 GHz range has been selected, with 10 GHz frequency is set as the initial design point for calculations. The wavelength of the antenna is then determined to be $\lambda = 3$cm.

3.1.2 Substrate Selection

One material that has proven compatible in high frequency designs and the growth

of graphene monolayers is quartz which has a relative permittivity, ε_r , of 3.9 and a loss tangent of $\delta \leq 0.0001$ at 30GHz. Quartz can be purchased in a variety of thicknesses, lengths, and width. Tjos antenna is designed with a substrate of 0.5 mm thickness to avoid loss associated with thick substrate materials.

3.1.3 Calculation

Once the operating frequency, thickness, and electronic parameters are known a patch antenna can be designed. Using well known formulas, the length and width of a patch antenna can be easily determined [13].

$$\epsilon_{reff} = \frac{\epsilon_r + 1}{2} + \frac{\epsilon_r - 1}{2}\left[1 + 12\frac{h}{W}\right]^{-\frac{1}{2}} \tag{3.1}$$

$$\frac{\Delta P_l}{h} = 0.412\frac{(\epsilon_{reff} + 0.3)\left(\frac{W}{h} + 0.264\right)}{(\epsilon_{reff} - 0.258)\left(\frac{W}{h} + 0.8\right)} \tag{3.2}$$

$$P_l = \frac{1}{2f_r\sqrt{\epsilon_{reff}\sqrt{\mu_0\epsilon_0}}} - 2\Delta P_l \tag{3.3}$$

$$P_w = \frac{1}{2f_r\sqrt{\mu_0\epsilon_0}}\sqrt{\frac{2}{\epsilon_r + 1}} \tag{3.4}$$

Using equations 3.2 through 3.4 the values for effective permittivity, patch length, and patch width can be obtained. The results of the selected substrate, substrate thickness, and operating frequency are described in Table 3.1. The calculated values for length and width

	$\varepsilon_{\text{reff}}$	ΔP_l	P_l	P_w	S_l	S_w
Calculate Values	3.482	2.32x10^{-4}	7.527	9.7	20	20
Fabrication Values	3.482	2.32x10^{-4}	7.5	9.5	20	20

Table 3.1: Patch antenna parameters in mm

of the antenna are within limits specified in the fabrication process however, dimensions are selected in increments of 0.5 mm to allow for clean fabrication of the patch antenna. The resulting dimensions are then estimated to be L = 7.5 mm and W = 9.5 mm. This change

will represent a shift in operating frequency and increase the reflection coefficient.

3.1.4 Antenna Feed

Patch antennas can be connected to signal generators or radio frequency systems in a myriad of ways. One popular method of feeding a patch antenna is from a signal generator is a probe feed. In this method a probe is attached to the patch antenna's metal through a via, or hole, in the substrate. Probe feeding is not viable in this instance due to the fragile nature of the quartz glass substrate.

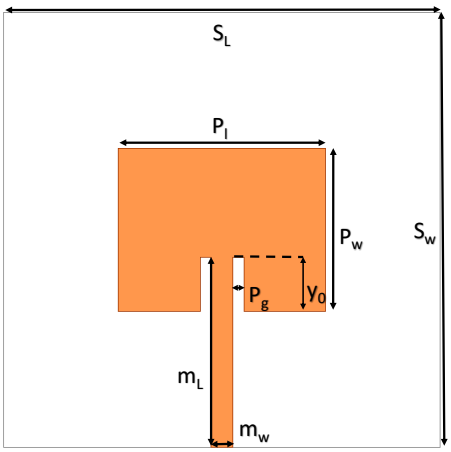

Fig. 3.1**:** Inset-fed antenna geometry with dimensions

Alternatively this project was designed to feed the patch antenna with an inset-feed due to relative simplicity in the design and fabrication process. As seen in figure 3.1 a micro-strip line is fed into a gap created in the body of the antenna. The inset feed is designed to match the antenna's input impedance to the signal source.

3.1.5 Micro-strip line

RF signal sources, generators, and network analyzers, are designed with 50 Ω output impedance. To feed the antenna a micro-strip transmission line is designed to be 50 Ω impedance. The microstrip line is created using standard formulas, then verified with

Agilent Advanced Design System (ADS).

$$Z_0 = \begin{cases} \frac{60}{\sqrt{\epsilon_{eff}}} \ln\left(\frac{8h}{W} + \frac{W}{4h}\right), & \text{for } W/h \leq 1. \\ \frac{120\pi}{\sqrt{\epsilon_{eff}}\left[\frac{W}{h} + 1.393 + 0.667 \ln\left(\frac{W}{h} + 1.44\right)\right]}, & \text{for } W/h \geq 1. \end{cases} \tag{3.5}$$

Using equation (3.5) the ratio of height and width can be expressed by equation (3.6)

$$\frac{W}{h} = \begin{cases} \frac{8e^A}{e^{2A}-2}, & \text{for } W/h < 2 \\ \frac{2}{\pi}[B - 1 - \ln 2B - 1 + \frac{\epsilon_r - 1}{2\epsilon_r}(\ln B - 1 + 0.39 - \frac{0.61}{\epsilon_r})], & \text{for } W/h > 2 \end{cases} \tag{3.6}$$

Setting h = 0.5 mm and $\varepsilon_{\text{eff}} = 3.482$ yields: W = 1.07 mm. Again the value obtained will be approximated to be 1mm to fit within the fabrication process limits. The transmission line is verified through an ADS simulation. The setup for the ADS simulation is shown in Figure 3.2.

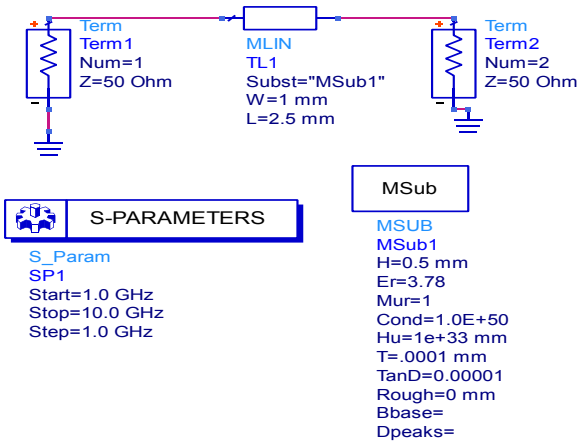

Fig. 3.2: ADS simulation setup

The results of the simulation, seen in Figure 3.3, show that over the 1-10 GHz band that the designed micro-strip line is transmitting at full power from port 1 to port 2. The results confirm that the designed microstrip transmission line is of 50 Ω impedance.

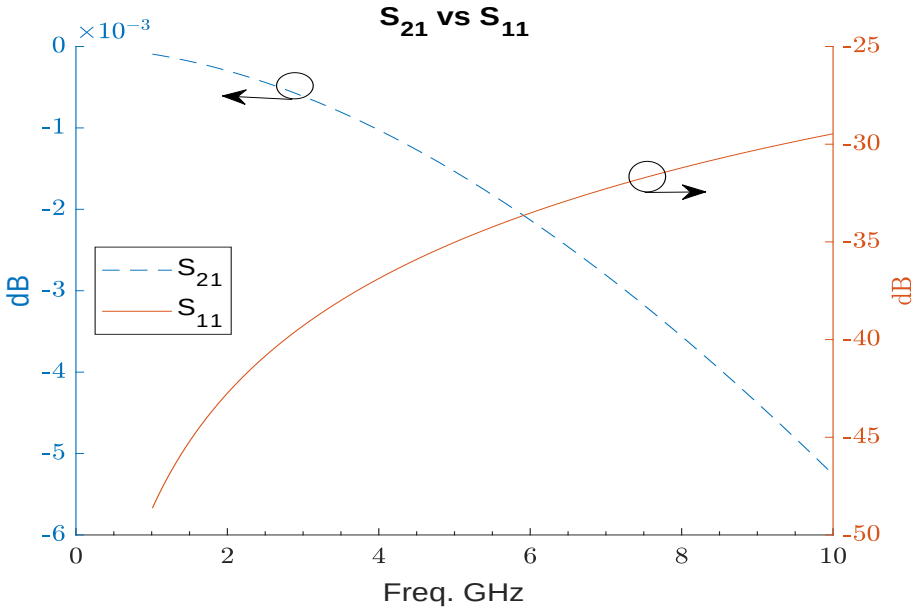

Fig. 3.3: Reflection and Transmission coefficient results from ADS for designed μStrip line

3.1.6 Inset Gap

With the micro-strip feed designed the gap and feed location can be determined. The gap or notch in the antenna plays a role in determining the resonant frequency and bandwidth of the antenna [14]. A gap values of 0.5 mm was selected, which is some fraction of the micro-strip feed width. The chosen value limits the bandwidth of the antenna but stays within the dimensional limit. Next the antenna body is matched to the 50 Ω microstrip line. The input impedance of the patch antenna at the edge is determined by equations (3.7)-(3.9) [13]:

$$R_{in} = \frac{1}{2(G_1 \pm G_{12})} \tag{3.7}$$

$$G_1 = \begin{cases} \frac{1}{90}\left(\frac{W}{\lambda_0}\right)^2, & \text{W} << \lambda_0 \\ \frac{1}{120}\left(\frac{W}{\lambda_0}\right), & \text{W} >> \lambda_0 \end{cases} \tag{3.8}$$

$$G_{12} = \frac{1}{|V_0|^2} Re \int_0^{\pi} [\frac{\sin\left(\frac{k_0 W}{2}\cos\theta\right)}{\cos\theta}]^2 J_0\left(k_0 L \sin\theta\right) \sin^3(\theta)\, d\theta \tag{3.9}$$

Solving for equations (3.8) - (3.9) first, then equation (3.7) yields: Using the results in Table

G_1	G_{12}	R_{in}
.001	$5.855\text{x}10^{-4}$	306.69Ω

Table 3.2: Conductivity and Input Impedance

3.2 a value for the inset feed location is then determined using equation (3.10):

$$50\Omega = R_{in} \cos\left(\frac{\pi}{L} y_0\right) \tag{3.10}$$

Finally, y_0 is determined to be 2.7mm analytically and estimated down to 2.5mm to match the fabrication processes.

P_l	P_w	y_0	m_w	P_g	S_l	S_w
7.5mm	9.5mm	2.5mm	0.5mm	1mm	20mm	20mm

Table 3.3: Patch antenna fabrication parameters

3.2 ANSYS High Frequency Structure Simulation

Using the values from Table 4.1 and the simple inset fed patch antenna geometry, the design can be further verified and modified to produce reliable and robust results. ANSYS High-Frequency Structure Simulator (HFSS) is used to simulate the real world performance of the designed patch antenna. The simulation is performed by using the built-in computer aided drafting (CAD) system, next excitations and boundary conditions are assigned to the geometry. All metallic elements were set to be perfect electric conductors (PEC). Dielectrics are manufacturer provided values for quartz and the excitation is assigned as a lumped port which is set to 50 Ω impedance. Though the initial results for this patch antenna exhibit poor performance, it is later improved by the addition of a parasitic layer, and further optimized in HFSS.

3.2.1 HFSS Results and Discussion

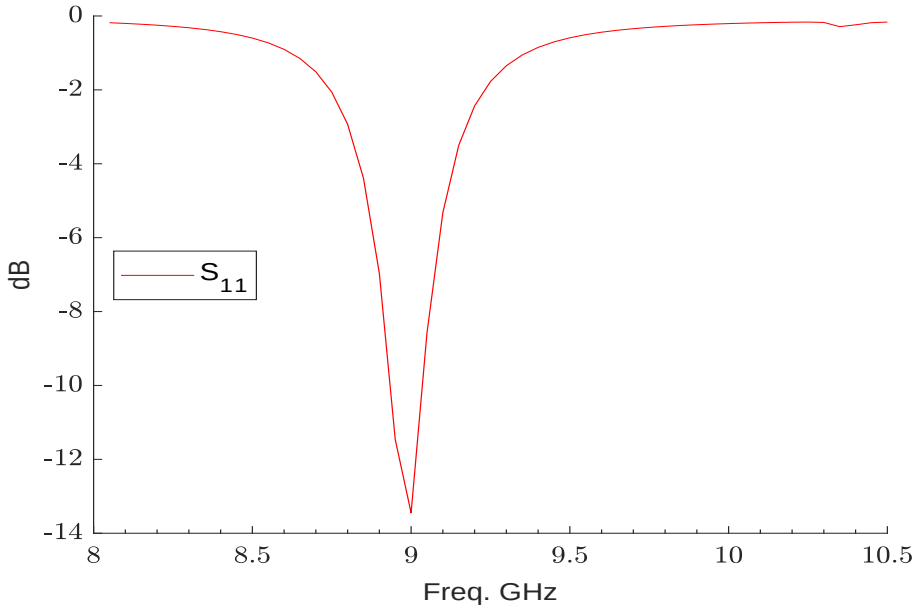

Fig. 3.4: Reflection Coefficient Plot

The S_{11} results in Figure 3.4, exhibit low performance for a single patch and are matched to 9 GHz. The results were expected due to the dimension limiting of 0.5 mm. The result in Figure 3.4 can also be explained by the resolution of the simulation frequency step of 0.05 GHz. Though the frequency step is small compared to the resonant frequency it still leaves smaller order frequencies uncalculated; however, the radiation pattern in this case is of more interest than that of the reflection coefficient plot. The radiation pattern, in Figure 3.6 shows a maximum gain value of 7dB at $\Theta = 00^{\circ}$ which is a uniform pattern as designed.

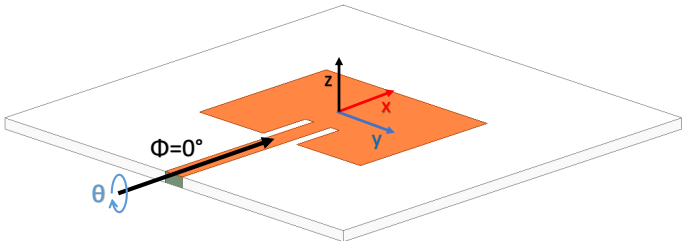

Fig. 3.5: Description of patch antenna geometry in relation to measurement angle, and Cartesian axis

The uniform pattern is ideal for beam steering applications as it provides an undisturbed structure from which beam steering performance can accurately be measured.

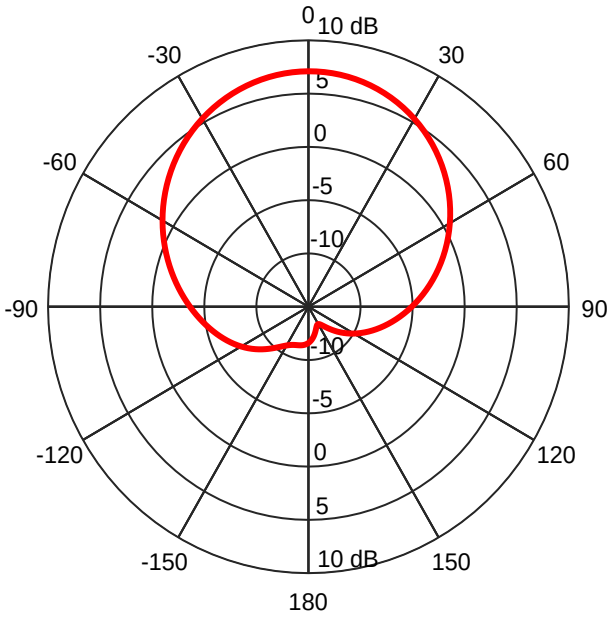

Fig. 3.6**:** Antenna Radiation pattern viewed at $\Phi = 0°$ with a maximum 7dB at $\Theta = 0°$

The measurement angle of $\Phi = 0°$ is in Fig. 3.5 along side of the patch antenna geometry. this measurement angle is help constant for the entirety of the the work in this thesis.

The results are improved later by the addition of a parasitic layer and parasitic elements as outlined in Chapter 4. The parasitic layer is split into two separate cases; zero spacing and dielectric, that are further discussed in Chapter 4. Each design case, zero spacing, and thick dielectric, influence the reflection coefficient and resonant frequency of the antenna design.

CHAPTER 4

Parasitic Layer Design

In MRA antenna design it is optimal to have a reconfigurable metallic layer that allows for antenna beam steering. This layer is designed by spacing metallic pixel elements similar to a Yagi-Uda antenna that was recently demonstrated by Towfiq, Bahceci, et. al [2]. MRA beam steering provides a method of achieving high gain in specified directions. This is highly desirable as beam steering can be used in applications well beyond the 5G wireless standard. In this chapter a parasitic layer is developed for future monolithic integration of graphene NEMS switches. TaN bias lines are also studied.

In this MRA a dielectric surface was used to support metallic pixel elements [2] that are used for antenna beam steering. Typically the two surfaces, driven element antenna and the parasitic surface are separated by an air layer that functions as a low loss medium as seen in Figure 4.1; however, it is also possible to separate the two layers by letting the thickness of the parasitic layer dielectric extend to the driven antenna element layer. In this chapter the design of both an air separated and thick dielectric spacing design will be discussed.

4.1 Design Considerations

In high-frequency MRA design it is necessary to use thin low loss dielectric media to provide support for the antenna and parasitic layer. A system that is compatible with graphene growth for future NEMS monolithic integration is also optimal. As discussed in Chapter 3 a quartz glass substrate is to be used due to its low loss nature at high frequencies and compatibility with graphene growth. Due to the fragile nature of a glass substrate care must be taken in the design and fabrication of the device.

4.2 Air Spaced Design

In most MRA designs the parasitic and driven element layer are separated by a thin layer of air. In this approach the air spacing holds, but, special manufacturing techniques and support structures will be needed to fabricate the final device.

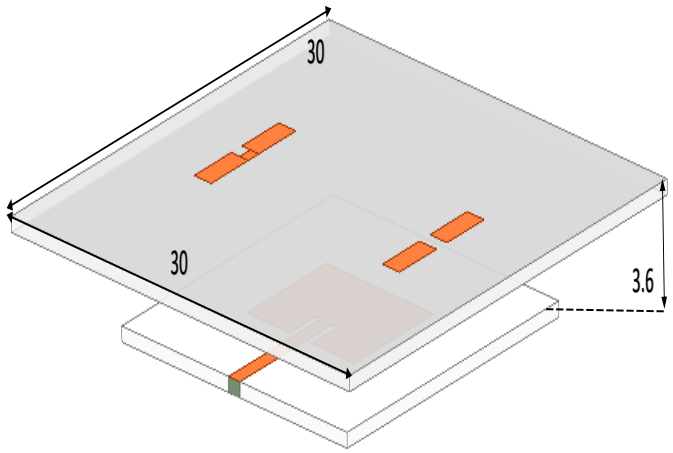

Fig. 4.1**:** Air spaced geometry

4.2.1 Parasitic Layer Spacing

In typical MRA's, the parasitic elements are spaced away from the driven element by some fraction of the wavelength, in this instance, values from 0.12 λ - 0.24 λ are chosen. In this design the spacing was set at 0.12 λ from the driven element layer to the parasitic surface. This value is consistent with typical Yagi-Uda antenna parasitic spacing [].

4.2.2 Parasitic Elements

With the spacing between substrate layers established it is possible to choose the parasitic element spacing, width, and length. The total connected element length was measured at ≈ 8 mm. The elements were then broken into 3.5 mm sized pixels, separated by 1 mm of space, designated for future switching devices.

4.2.3 Modes

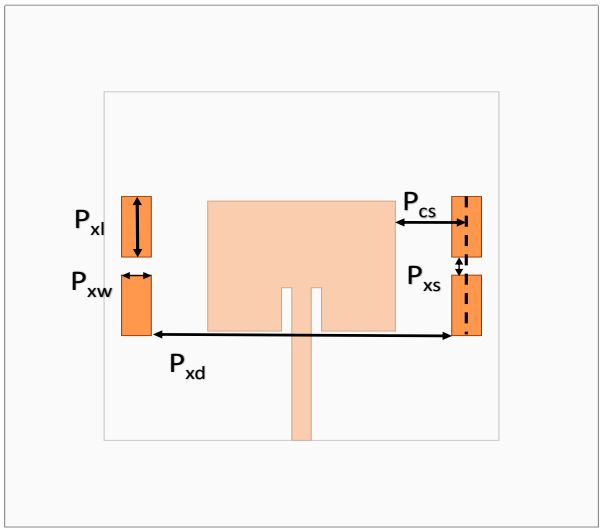

Fig. 4.2: Air Spaced Design Parasitic layer

P_{xl}	P_{xw}	P_{xs}	P_{xd}	0.12λ
$.116\lambda = 3.5mm$	$0.05\lambda = 1.5mm$	$0.03\lambda = 1mm$	$0.5\lambda = 15.2mm$	3.6mm

Table 4.1: Patch antenna fabrication parameters

An MRA antenna design exhibits different modes of operations dependent upon the number of beam steering elements. In this design there are two beam steering elements, each is divided into two pixels, and placed symmetrically about the x-axis on the parasitic surface. The device then exhibits two modes of operation: Mode 0 and Mode 1. Mode 1 is seperated into two cases symmetric at the x-axis: left, and right. Each of the corresponding modes have been studied in HFSS.

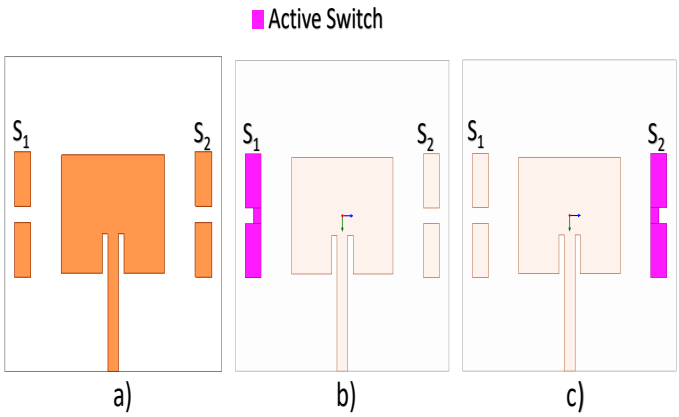

Fig. 4.3**:** Air Spaced MRA (a) Mode 0: S_1/S_2 off (b) Mode 1 Left: S_1 on, S_2 off (c) Mode 1 Right: S_1 off, S_2 on

4.2.4 Results and Discussion

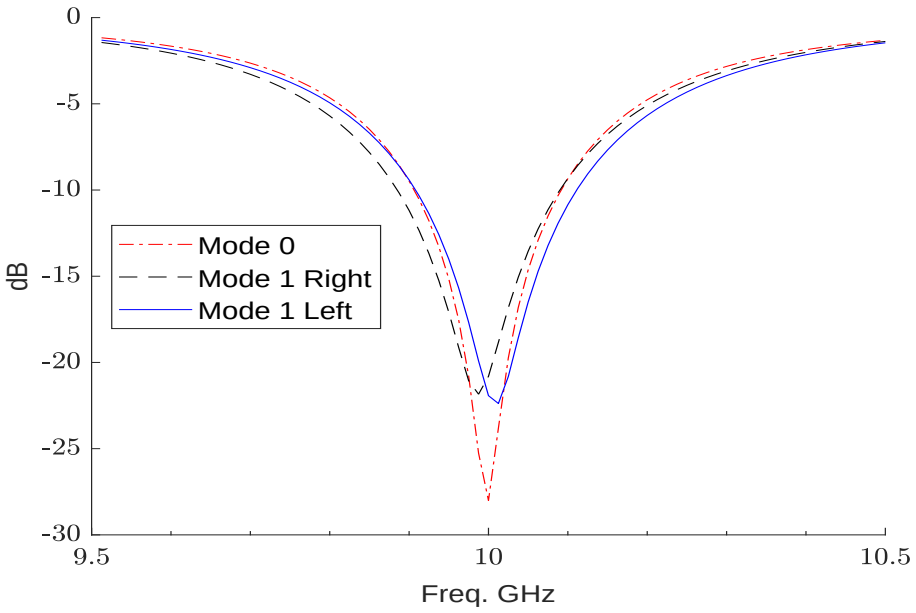

Fig. 4.4**:** Reflection coefficient plot for all modes of the Spaced MRA

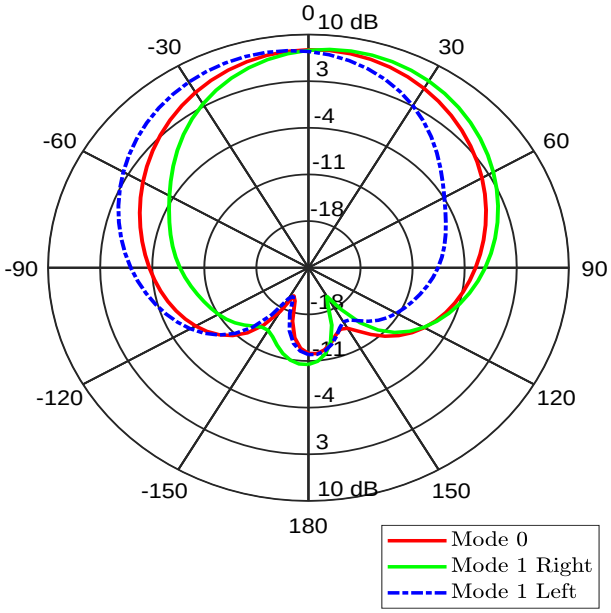

Fig. 4.5**:** Spaced MRA Radiation Pattern of all three modes

Though the design achieves reasonable performance, and can be manufactured, the fragile nature of the glass substrate is still a concern. However, this does provide a fair comparison to our previous MRA designs [2]. Though comparable to older MRA designs, the air spacing technique may fail at frequencies where the required spacing between the parasitic layer and driven element may be decreased even further.

4.3 Dielectric MRA Design

It was determined to use a dielectric layer placed directly onto the radiating body to support the parasitic elements. In this tesign the dielectric layer is in direct contact with the driven element, as reflected in Figure 4.7. The parasitic layer has a thickness that is equal to the driven element substrates which results in the advantage of this design is that no special holding apparatus is needed for spacing between the two glass layers.

4.3.1 Parasitic Dielectric Thickness

The spacing between the parasitic elements and the driven layer is chosen to be 0.5 mm In contrast to previous MRA designs. This value was chosen since the driven elements

substrate was already 0.5 mm which limited the number of specific components in the design.

4.3.2 Parasitic Element Design

The parasitic elements are designed by first obtaining the quarter-wavelength monopole element length which is determined to be 7.5 mm. This length is then divided among a set of unconnected metallic patches on the parasitic surface layer. The two parasitic elements or pixels are separated by 1 mm distance which equate to a total length of 7.5 mm when connected. As with the Air Spaced MRA design, elements are set to be 1 mm in width.

4.3.3 Parasitic element placement

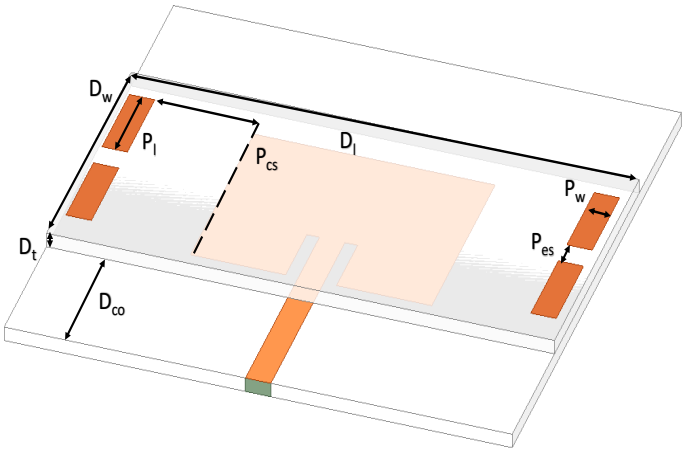

Fig. 4.6**:** Dielectric MRA with dimensions

D_w	D_t	D_l	P_{eo}	D_{co}	P_l	P_{cs}	P_w	P_s
10	0.5	20	0.35	5	2.25	3.9	1	1

Table 4.2: TD MRA dimensions in mm

The distance between the radiating body and pixel elements, in $\hat{y}$ direction, is set to be at 0.13 λ. This value mirrors the dielectric layer's thickness and is consistent with

classic Yagi-Uda designs. The total geometry can be seen in Figure 4.7. The design is then simulated in HFSS to obtain results for the S_{11} and radiation pattern behaviors.

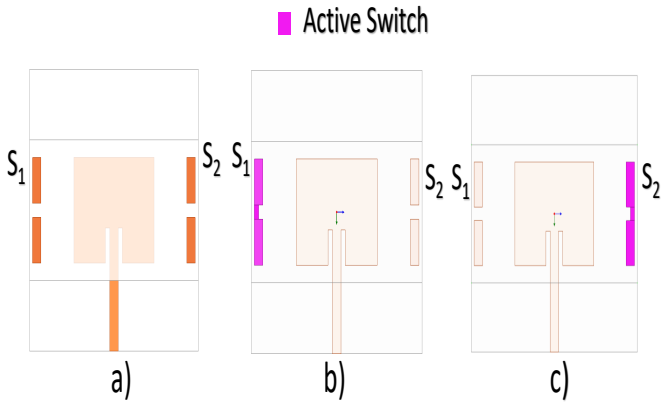

Fig. 4.7: Dielectric MRA modes (a) Mode 0: S_1/S_2 off (b) Mode 1 Left: S_1 on, S_2 off (c) Mode 1 Right: S_1 off, S_2 on

4.3.4 Results and Discussion

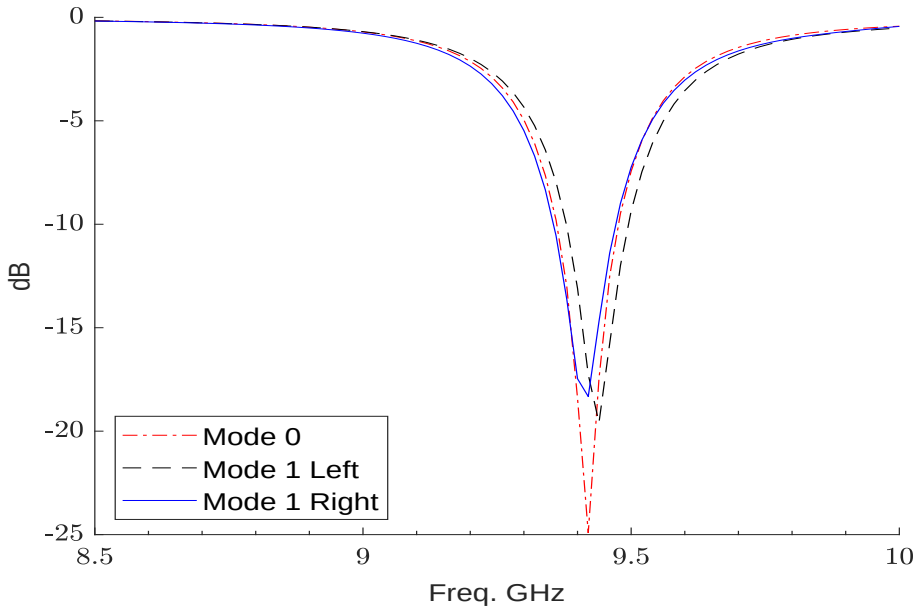

Fig. 4.8: S_{11} plot of Thick Dielectric MRA

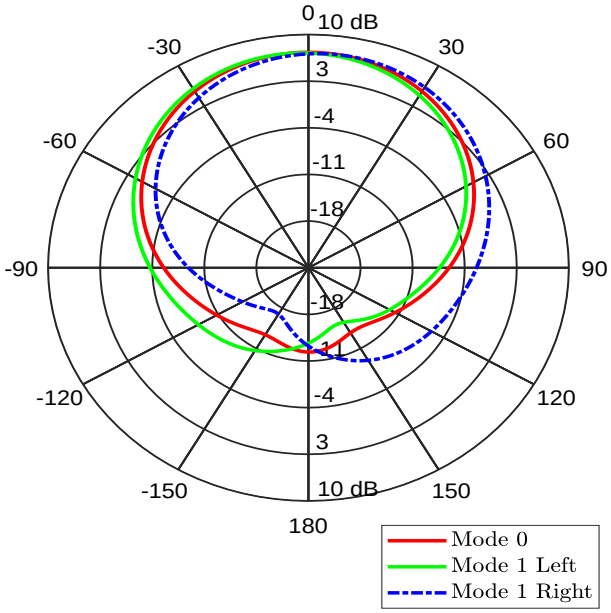

Fig. 4.9**:** Radiation pattern of Dielectric MRA

The plot displayed in Figure 4.8 shows that the reflection coefficient of this design is of acceptable value for Mode 0. In Figure 4.9 it can be observed that the realized gain for all modes is above 7 dB which is desired for a patch antenna.

Mode	Critical Freq.	dB_{max}	Θ_{max}
Mode 0	9.38 GHz	7.3	0°
Mode 1 Left	9.44 GHz	7.3	-8°
Mode 1 Right	9.42 GHz	7.3	8°

Table 4.3: Dielectric MRA Design Results

4.4 Final Discussion

In this chapter the MRA, without switches, is finalized and shows reasonable performance for future use in research. The two designs shown, provide a method of comparison between air spaced MRAs and dielectric MRA designs. Both designs can be used to perform beam steering.

4.4.1 Conclusion

Section 4.2 lays out the design of a classic air spaced MRA [2]. This MRA has been widely studied but fails due to the specific design parameter of the spacing requirements between driven and parasitic layers. Keeping this failure in mind the fragile nature of quartz glass was of great concern in the mechanically separated layers. Both designs show reasonable steering and can be used in future works. The Dielectric MRA shows advantage over the Air Spaced MRA in that it does not need mechanical separation and can be easily fabricated.

CHAPTER 5

Tantalum Nitride Bias Lines

In the design of radiating systems and communications equipment an ever-increasing challenge is the need for conductive materials that do not affect the performance of wireless systems. One material that can be used in an antenna system, such as an MRA, is tantalum nitride (TaN). TaN is of particular interest for the use in high-frequency MRA design due to its high value of resistivity. In this chapter TaN is investigated as a dc bias line for pixel element switching.

5.1 Design

MRA switching elements are placed between parasitic pixels. The placement limits the length, amounts and types of metals used for dc electrodes in MRAs. It has been proposed conceptual future NEMS development design a dc bias line is routed beneath the switching element as seen in chapter 8. A way to reduce the impact of the dc bias lines on the MRA antenna is to design these lines with TaN.

In the fabrication process the dimensions are limited to 100 μm, therefore the TaN bias lines are designed to be compatible with this process. The width of the dc bias lines are set to be 200 μm, which will provide some room for fabrication error in both the spacing between pixels and deposition of the TaN material for the bias lines.

5.1.1 Total Physical Layout

The TaN bias lines that are designed on top of the MRAs discussed in chapter 4 illustration of the geometry of each case Spaced and Dielectric MRA as seen in Figure 5.1 and Figure 5.2. The TaN bias lines are intentionally run directly above the driven patch element to maximize the interference of the bias lines. The routing is done to highlight both the impact of low resistivity materials and the minimal impact of highly resistive materials.

It has been conceptually proposed that in future NEMS development and design a dc bias line is routed beneath the switching element (Chapter 8) and connected to an external contact pad as in in Figure 5.1 and Figure 5.2 that controls the MRAs operating mode.

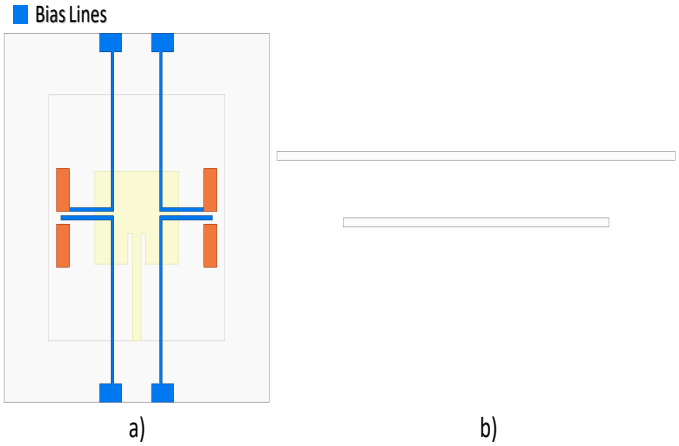

Fig. 5.1**:** TaN bias line geometry on the Spaced MRA

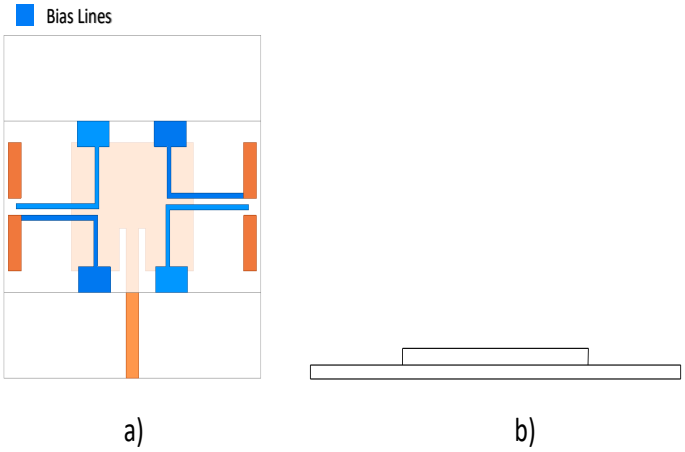

Fig. 5.2**:** TaN bias line on the Dielectric MRA

5.2 Simulation

Simulations are performed to understand the affect of TaN bias lines on the layout described in subsection 5.1.1. The simulation is run using resisitvity values as specified in

Table 5.1. The values for resisitivity were obtained by Dr. T.-C. Shen at the Nano-Device Labratory (NDL) [15]. The simulations are setup to explore Mode 0, Mode 1 Left, then

Resistivity	Sheet Resistance
$3.1\text{x}10^{-4} - 5.1\text{x}10^{0}\Omega - cm$	$2.7\text{x}10^{1} - 4.4\text{x}10^{5}\Omega/Sq.$

Table 5.1: NDL obtained TaN material resistivity

Mode 1 Right with sheet resistance values from Table 5.1. As a control the bias lines are also set to have sheet resistance of 500 nm thick copper (Cu), 0.0336 Ω/Sq. which helps illustrate the impact of highly resistive dc bias lines in MRA designs.

5.3 Air Spaced MRA

The Air Spaced MRA is considered first, as in Chapter 4, and each of its modes are presented.

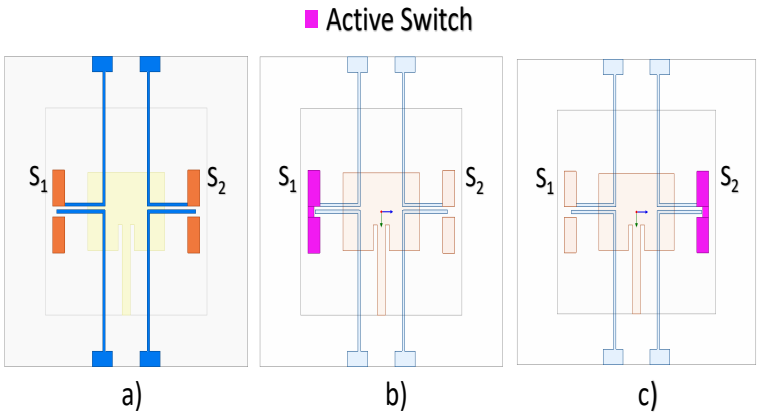

Fig. 5.3**:** Air Spaced MRA with TaN bias lines (a) Mode 0: S_1/S_2 off; (b) Mode 1 Left: S_1 on, S_2 off; (c) Mode 1 Right: S_1 off, S_2 on

5.3.1 Mode 0: S_1/S_2 off

In Mode 0 there is some distortion from the bias lines present in both the radiation pattern and the reflection coefficient plot. In Figure 5.5 the Cu bias lines reflect the radiation lowering Mode 0's performance by 5 dB. It can also be seen in Figure 5.4 that the higher

impedance bias lines have significantly less of an impact on the S_{11} performance.

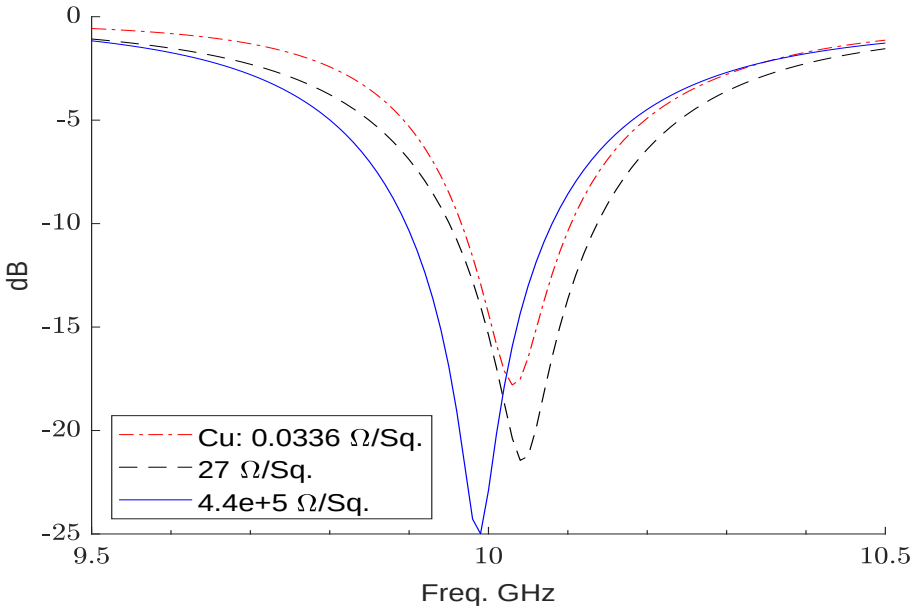

Fig. 5.4**:** Air Spaced MRA Design Mode 0: S_{11},

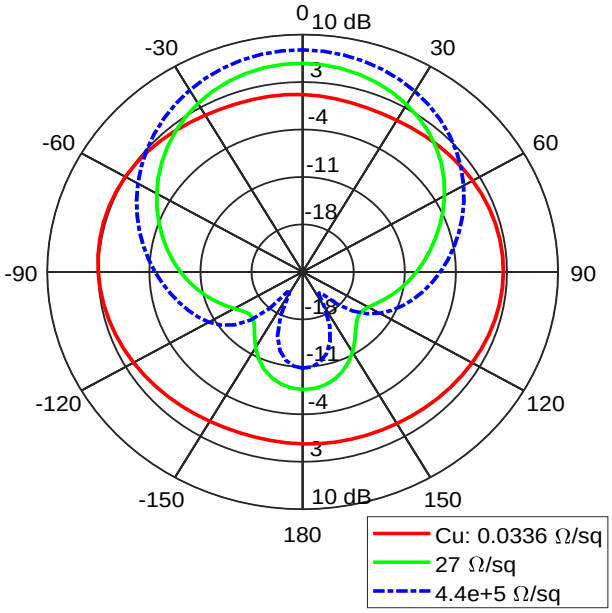

Fig. 5.5**:** Air Spaced MRA Design Mode 0: S_1/S_2 off, where each pattern is measured at its resonant frequency

Mode 0	Critical Freq.	θ_{max}	dB_{max}
Cu: 0.0336 Ω/Sq.	10.03 GHz	-5°	3.3
27 $\Omega/Sq.$	10.04 GHz	0°	5.8
4.4x10^5 $\Omega/Sq.$	9.99 GHz	0°	7.8

Table 5.2: Performance of Cu and TaN sheet resistances for Air Spaced MRA: Mode 0

5.3.2 Mode 1 Left and Right: S_1 on, S_2 off and S_1 off, S_2 on

Mode 1 is studied similar to the Mode 0 with the inclusion of a short between adjacent pixels that is of zero resistance value. It can be seen in both left and right patterns that the highly resistive bias line presents the least pattern deformation and the lowest value for S_{11}. The S_{11} result is a definite indication that the TaN bias lines will work on a parasitic MRA surface without adversely affecting the maximum gain in beam steering modes.

It can also observed that the Cu bias lines have deformed the pattern, but maintain a reasonable S_{11} value. This also shows that replacing Cu dc bias lines with TaN improves the overall performance of the classic Air Spaced MRA designs.

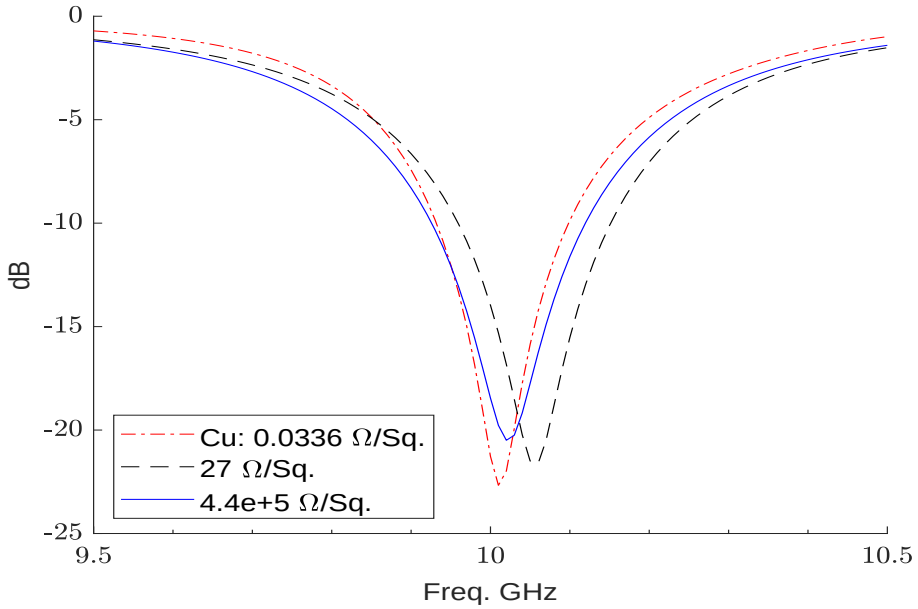

Fig. 5.6: Air Spaced MRA Design Mode 1 Left

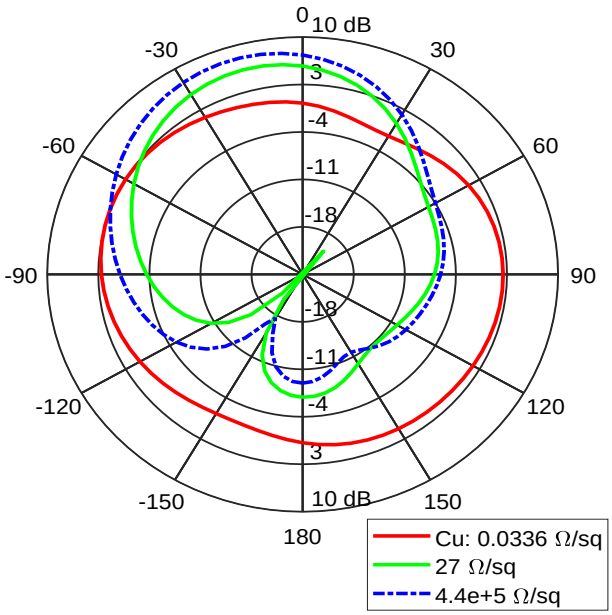

Fig. 5.7**:** Air Spaced MRA Design Mode 1 Left: S_1 on where each pattern is measured at its resonant frequency

Mode 0	Critical Freq.	θ_{max}	dB_{max}
Cu: 0.0336 Ω/Sq.	10.05 GHz	-65°	3.1
27 $\Omega/Sq.$	10.08 GHz	-15°	6.3
4.4x10^5 $\Omega/Sq.$	10.04 GHz	-15°	8.1

Table 5.3: Performance of Cu and TaN sheet resistances for Air Spaced MRA Mode 1 Left

Mode 0	Critical Freq.	θ_{max}	dB_{max}
Cu: 0.0336 Ω/Sq.	10.01 GHz	60°	3.5
27 $\Omega/Sq.$	10.04 GHz	20°	6.3
4.4x10^5 $\Omega/Sq.$	10.01 GHz	20°	8.2

Table 5.4: Performance of Cu and TaN sheet resistances for Air Spaced MRA Mode 1 Right

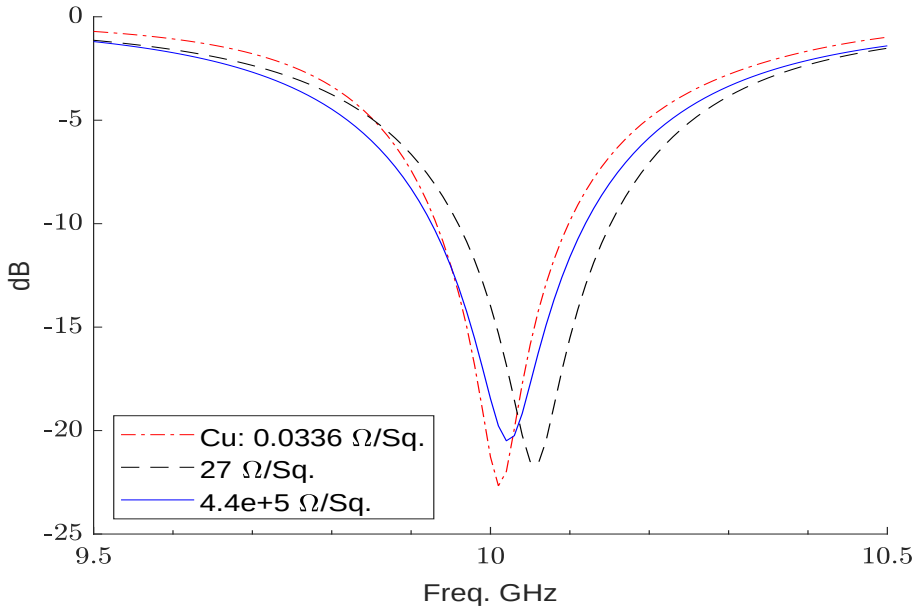

Fig. 5.8**:** Reflection Coefficient of Air Spaced MRA Mode 1 Right: S_2 on

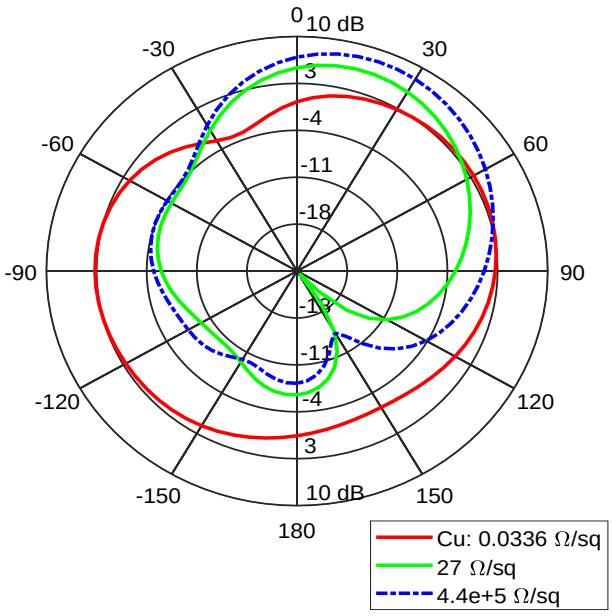

Fig. 5.9**:** Radiation pattern of Air Spaced MRA Mode 1 Right: S_2 on, where each pattern is measured at its resonant frequency

5.4 Dielectric MRA

The Dielectric MRA is studied for use with TaN bias lines. It is expected that the performance of the Dielectric MRA should mirror that of the air spaced MRA design, however, it is shown that this not the case. Explanations for this discrepancy will be presented in section 5.4.3.

5.4.1 Mode 0: S_1/S_2 off

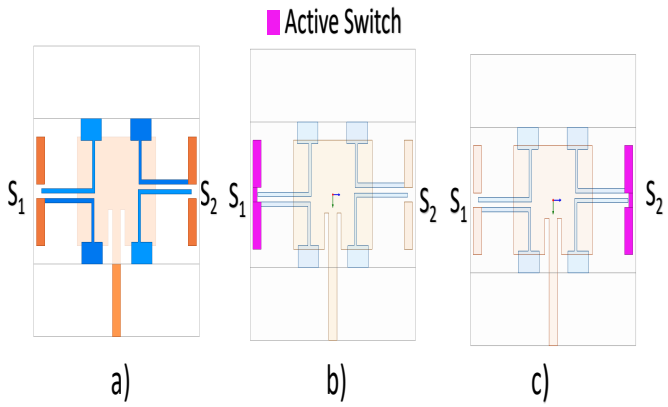

Fig. 5.10**:** Dielectric MRA with TaN bias lines (a) Mode 0: S_1/S_2 off; (b) Mode 1 Left: S_1 on, S_2 off; (c) Mode 1 Right: S_1 off, S_2 on

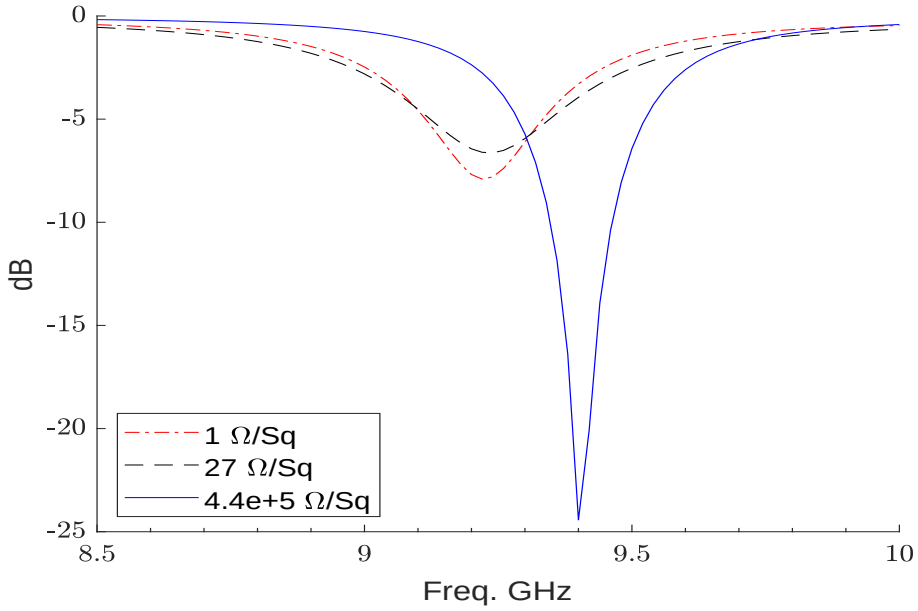

Fig. 5.11: Dielectric MRA Design Mode 0

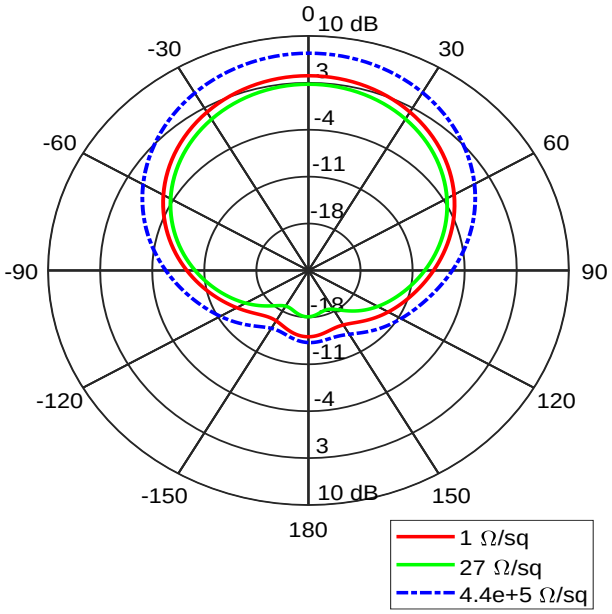

Fig. 5.12: Dielectric MRA Design Mode 0 where each pattern is measured at its resonant frequency

Mode 0	Critical Freq.	θ_{max}	dB_{max}
1 Ω/Sq.	9.22 GHz	0°	4.1
27 $\Omega/Sq.$	9.24 GHz	0°	2.8
4.4x10^5 $\Omega/Sq.$	9.4 GHz	0°	7.4

Table 5.5: Performance of Cu and TaN sheet resistances for Dielectric MRA Mode 0

5.4.2 Mode 1 Left and Right: : S_1on, S_2 off and S_1off, S_2 on

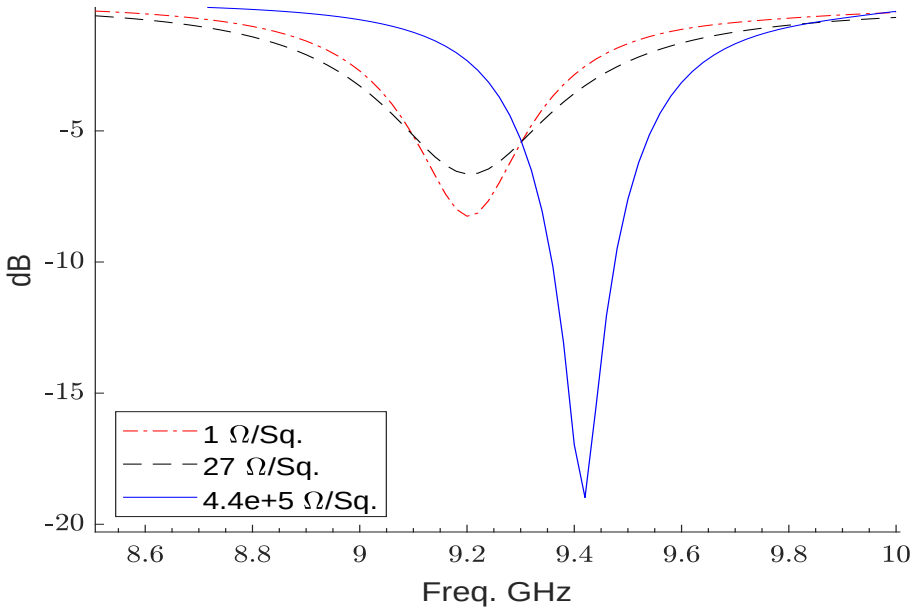

Fig. 5.13**:** Dielectric MRA Design Mode 1 Left

Mode 0	Critical Freq.	θ_{max}	dB_{max}
1Ω/Sq.	9.22 GHz	0°	3.5
27 $\Omega/Sq.$	9.26 GHz	-6°	2.9
4.4x10^5 $\Omega/Sq.$	7.3 GHz	-10°	7.3

Table 5.6: Performance of Cu and TaN sheet resistances for Dielectric MRA Mode 1 Left

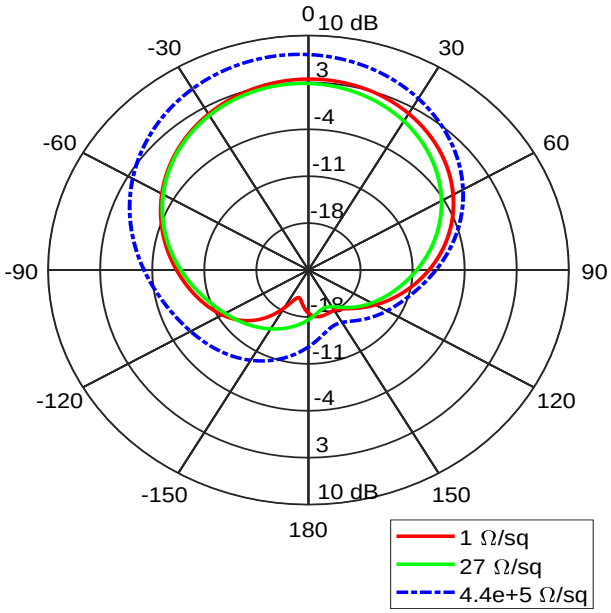

Fig. 5.14: Dielectric MRA Design Mode 1 Left Radiation Pattern, where each pattern is measured at its resonant frequency

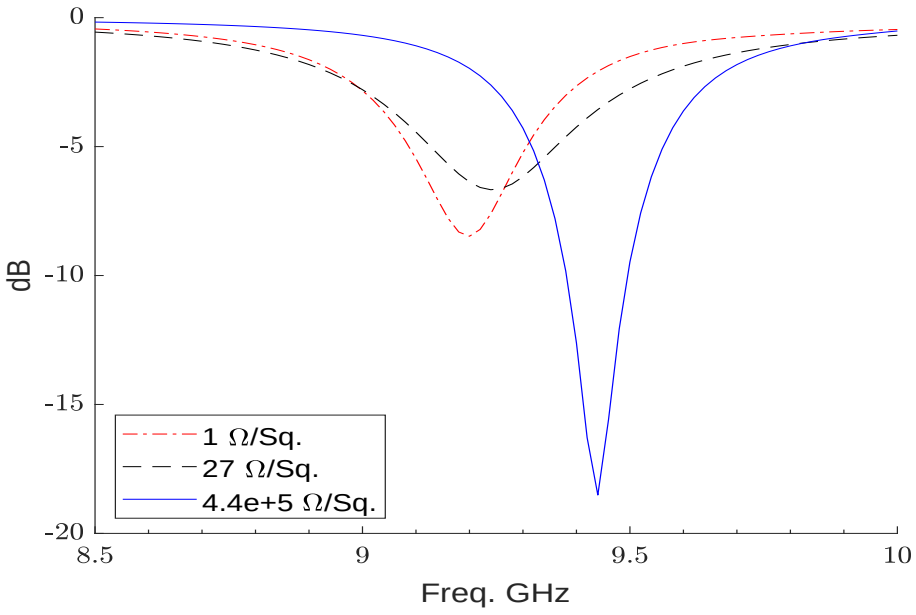

Fig. 5.15**:** Dielectric MRA Design Mode 1 Right

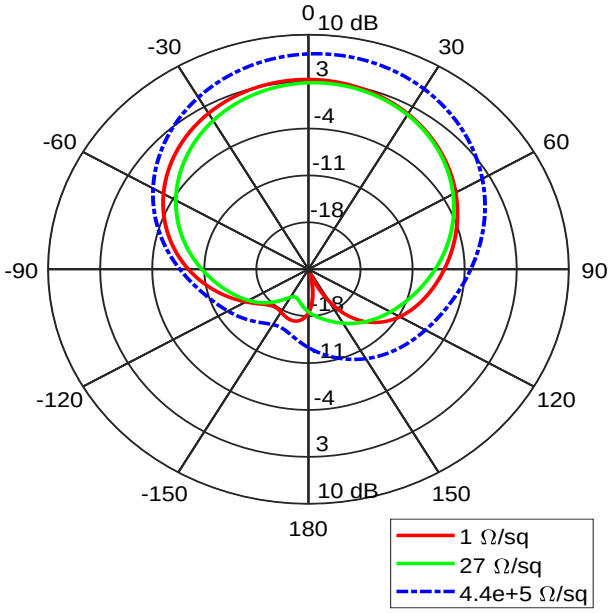

Fig. 5.16**:** Dielectric MRA Design Mode 1 Right Radiation pattern, where each pattern is measured at its resonant frequency

Mode 0	Critical Freq.	$\theta_{\max}$	$dB_{\max}$
1 Ω/Sq.	9.2 GHz	0°	3.3
27 $\Omega/Sq.$	9.24 GHz	6°	2.9
4.4x10^5 $\Omega/Sq.$	9.44 GHz	10°	7.2

Table 5.7: Performance of Cu and TaN sheet resistances for Dielectric MRA Mode 1 Right

5.4.3 Discussion

As seen in each of the Modes for the thick Dielectric MRA the lowest resistivity value metals exhibit lower gain. The lower gain is accompanied by a lack of steering for each mode due to the coupling of the patch antenna with the low resistivity metals. The high sheet resistance TaN bias lines show a high degree of steering accompanied by little to no impact on the gain value of the antenna.

5.5 Conclusion

In this chapter TaN dc bias lines were studied for use with MRA parasitic surfaces.

The Air Spaced MRA design displayed the greatest benefit with the use of highly restive metals. The Dielectric MRA showed a decreased in gain from low resistivity materials and presented little to no back steering when compared to that of the Air Spaced MRA design.

The TaN bias lines then have showed greater value in MRA antennas. With highly resistive dc bias lines MRA designs can further be compacted for use in smaller systems. This will also prevent deleterious effects from low resitivity metals. Additionally, the use of TaN bias lines shows promise for the application of graphene based NEMS devices.

CHAPTER 6

Co-planar Wave Guide to μStrip Transition Design

It is advantageous to fabricate NEMS devices for radio frequency systems due to the faster switching speed and high degree isolation NEMS devices presented [3]. In the development of future NEMS switches it is important to formulate a methodology to study the viability of the designed and fabricated devices. Therefore it is important to obtain the transmission and reflection measurements of the device with a network analyzer.

6.1 Equipment

At NDL there is a test setup for analysis of various RF devices using a Cascade Microtech EPS150MMW probe station. This station is designed to be used to connect semiconductor devices at micrometer scale and other pertinent test equipment. In this case the EPS150MMW can be used to interface between a micrometer scale RF device, a graphene NEMS switch, and a network analyzer.

6.1.1 Probe Head

Fabricated devices are connected to the probe station using a co-planar wave guide (CPW) probe head. A CPW probe head provides both the RF and ground signal. NDL currently has a set of GSG250 probe heads for use with the Cascade probe station. These probe heads have a SubMiniture version A style connector for the network analyzer, and a set of probe contacts. The probe contacts are in a CPW configuration where tip separation and contact tip width are designed, by the manufacturer, to be of 50 Ω impedance.

The specific dimensions are not readily available from the manufacturer website so a representative from Cascade was contacted to determine the correct dimensions [16]. The dimensions and probe head layout are depicted in Fig. 6.1 where signal paths are also identified.

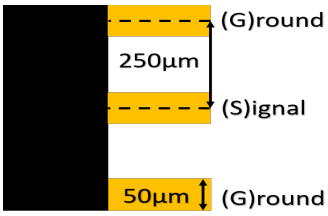

Fig. 6.1: Cascade GSG250 probe head with dimensions

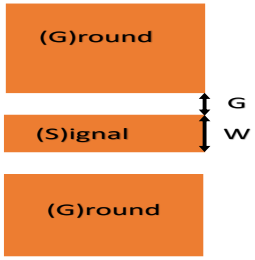

Fig. 6.2: Example of a CPW Transmission line

6.2 CPW transition design

Using the GSG probe head requires a set of CPW contacts on the fabricated device. The CPW contacts on the device must be designed to both fit the probe head dimensions, and also myst be of 50 Ω impedance to avoid signal reflection. Key parameters in the design of CPW transmission line are similar to that of the micro-strip line designed in Chapter 3, however the design of CPW transmission lines are significantly more complicated than that of micro-strip transmission lines, hence computer-aided design (CAD) tools were used [17].

The design of the NEMS devices explores the fabrication and testing of such devices on two substrates; Si with a SiO_2 interface layer (100-500 nm) and quartz. The quartz substrate was chosen for compatibility with graphene monolithic integration as in previous chapters. The Si/SiO_2 substrate was selected for the detectability of graphene monolayers using optical microscopy [18].

Both substrates have different permittivities and loss tangents. Table 6.1 lists the material specific properties used in the design and simulation of the CPW transmission lines. It is of note that the value used for Si/SiO_2 substrate is estimated to be just the values of an Si substrate

Additional care must be taken to design a CPW line that is compatible with the probe

	Quartz	Si
ε_r	3.78	11.7
tanδ	.0001	.004 [17]

Table 6.1: Quartz and Si dielectric properties

head. The conductors must be able to accommodate the full width of the 50 μm probe tip and allow for sufficient separation between adjacent conductors. From the dimensions seen in Fig. 6.1 maximum separation from each conductor must be no greater than 225 μm in distance.

6.2.1 LineCalc

Agilent ADS comes packaged with a transmission line calculation tool called LineCalc. In Chapter 3 ADS is used to simulate the micro-strip line that is designed for the antenna feed. LineCalc is then used to design the CPW transmission line that is fed into ADS to perform a quick simulation and HFSS will later provide full wave simulation of the final transition.

Using the values listed in Table 6.1 and the desired metal thickness of 500 nm, compatible CPW conductor spacing and widths appropriate for the measurement system can be found for an operating frequency of 10 GHz.

Values for both Si and Quartz based CPW designs are displayed in Table 6.2, they are then rounded up to whole integers in the μm range.

6.2.2 ADS Simulation Setup

Using the parameters calculated in the last section it is possible to simulate a CPW

Substrate	W	G	Ω
Quartz	152.69 μm	15 μm	50 Ω
Si	50.85 μm	30 μm	50 Ω
Quartz (rounded)	153μm	15 μm	49.97 Ω
Si (rounded)	51 μm	30 μm	49.95 Ω

Table 6.2: Calculated and Rounded CPW Transmission line values

to micro-strip transition inside of ADS. The two designs have nearly identical simulation setups so only one is presented, but, both designs are simulated and presented together in the following section. The final transition geometry can be found in Figure 6.4. Specific dimensions can be found in Table 6.3.

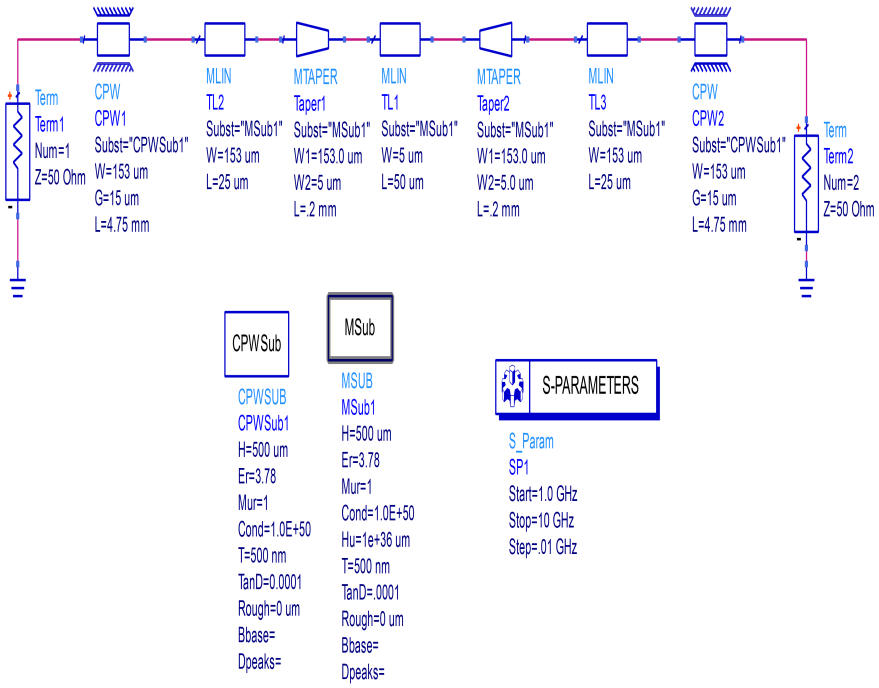

Fig. 6.3**:** ADS simulation setup for Quartz

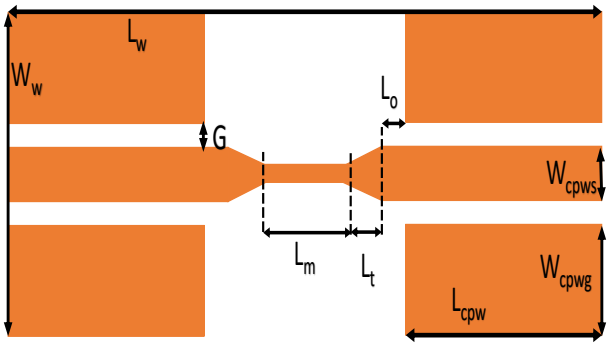

Fig. 6.4: Physical layout of CPW to $\mu Strip$

Substrate	L_w	W_w	G	L_m	W_m	L_t	L_{cpw}	W_{cpws}	W_{cpwg}	L_{open}
Quartz	10mm	10mm	$15\mu m$	$50\mu m$	$5\mu m$	$200\mu m$	4.75mm	153 μm	4.905mm	$10\mu m$
Si	10mm	10mm	$30\mu m$	$50\mu m$	$5\mu m$	$200\mu m$	4.75mm	$51\mu m$	4.94mm	$10\mu m$

Table 6.3: CPW to μStrip dimensions for Quartz and Si

6.2.3 ADS Simulation Results

The simulation from ADS is used as a first basis assessment of the quality of the transmission design and as a means to auto-generate the physical layout of the design. Each of the substrates is studied by evaluating the S_{11}, reflection coefficient, and S_{21} the power received at terminal 2.

6.3 HFSS

Using the transmission line transition modeled in the previous section, different operating modes, closed and open, can be studied. This is done in an attempt to model idealistic behavior of a NEMS switch which will serve as a means of comparison when the device is fabricated.

The design is imported to HFSS and placed onto square substrates, Si and quartz, then broken into the two individual operating cases. The two cases open and closed mimic the behavior of a NEMS switch. A basic design for the transition is displayed in Fig. 6.4 and Fig. 6.7.

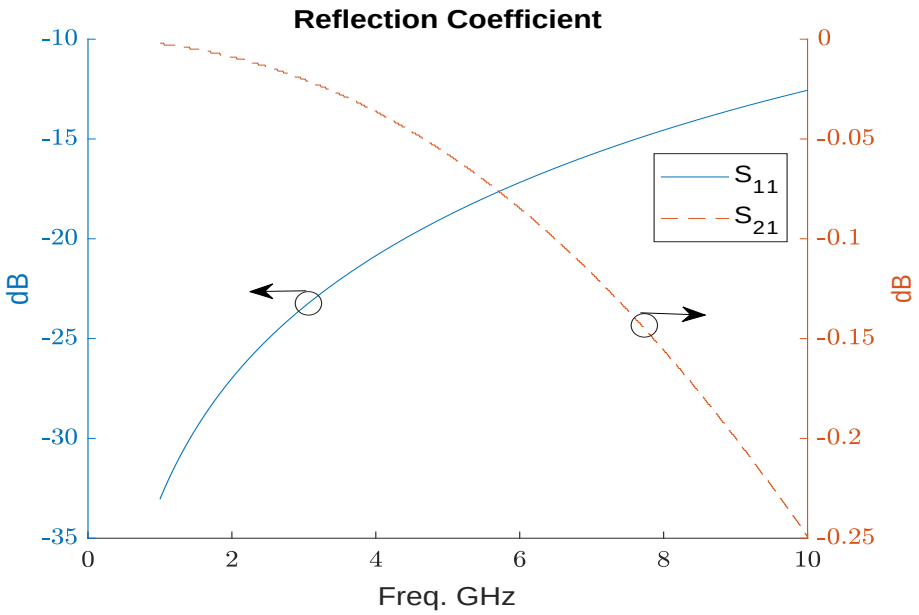

Fig. 6.5**:** ADS Simulation Results for the Quartz CPW to miro-strip design

6.3.1 Closed

The first, and easiest simulation, is to a fully closed switch. The layout is exported directly from ADS into HFSS, then re-simulated to re-verify the results obtained in ADS.

6.3.2 Open

The last simulation is needed to understand how the CPW transition line will behave when attached to a NEMS switch in the open configuration. In this configuration it is optimal to open the center micro-strip line by 10 µm. This dimension is chosen to mirror that of the conductor width presented by P. Sharma *et al.* [6].

6.4 Discussion

The results of the transmission line for both substrates show reasonable performance from 1 GHz to 10 GHz frequencies. In the case of our previously designed MRA antennas, operating at 8-10 GHz is desirable for the testing of graphene NEMS switches on parasitic surfaces. For the quartz based CPW transition design, the results are acceptable and can be used directly with graphene NEMS fabrication methods, however, the Si design exhibits

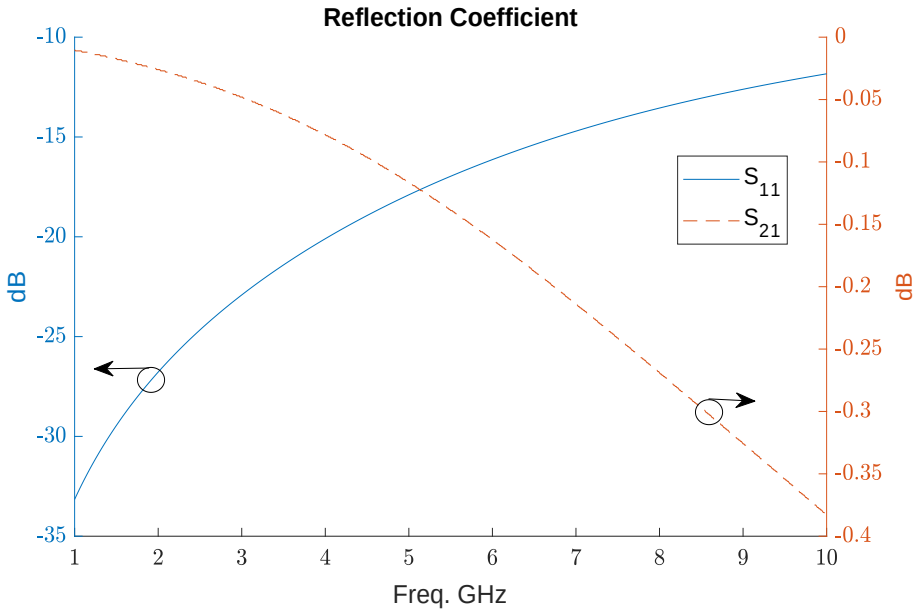

Fig. 6.6: ADS simulation results for Si CPW to micro-strip design

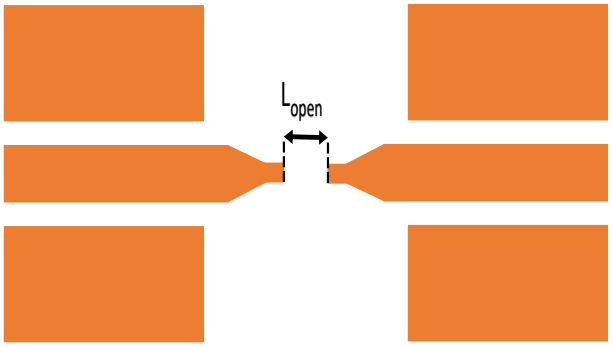

Fig. 6.7: Illustration of an opened transition

poor performance around 8-10 GHz for both open and closed switch cases. The results can be explained by first looking at Fig. 6.11 in the 8-10 GHz band of frequencies. It is noted that the reflection coefficient drops to less than -25 dB at 9.25 GHz. This effectively lets the CPW act as a micro-strip antenna on Si surfaces when set to the open configuration. Additionally, the element length of a patch antenna on Si at 9.25 GHz, can be calculated and measured at approximately 5 mm. So, to avoid loss of the magnitude displayed in Figures 6.9 - 6.11, the designs must not allow for lengths of 50Ω transmission lines that closely approaches that of patch element length.

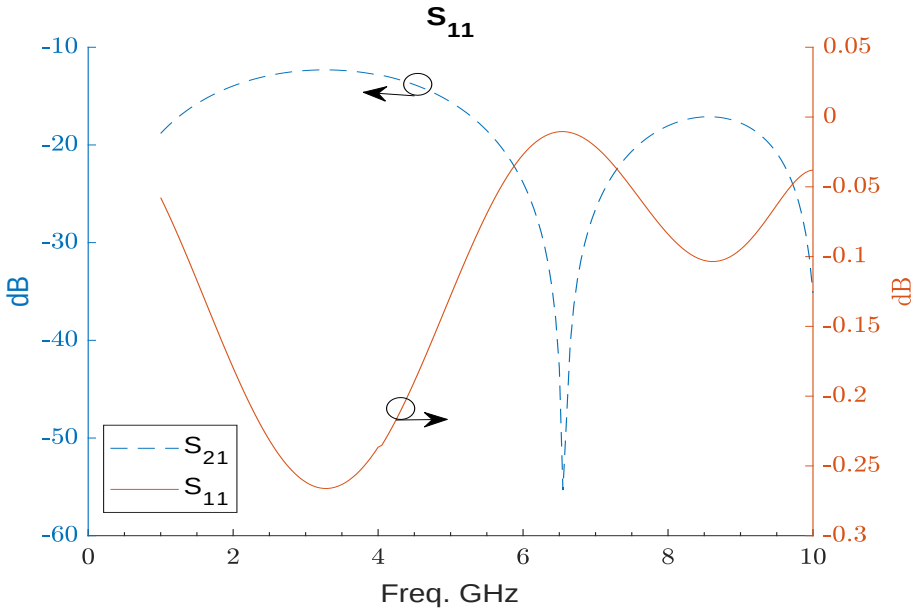

Fig. 6.8: HFSS simulation results for Quartz design in closed configuration

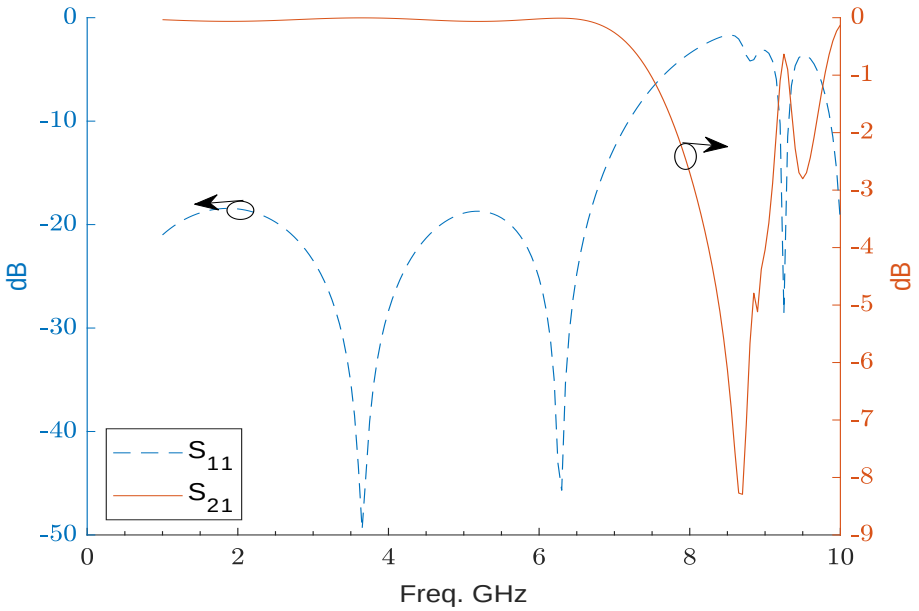

Fig. 6.9: Simulation Results for Si: Closed

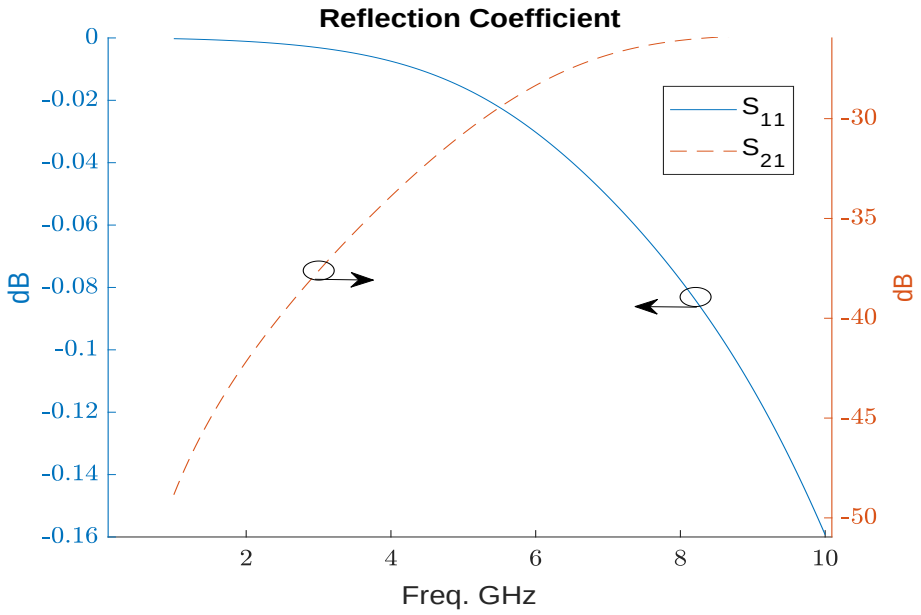

Fig. 6.10: Simulation Results for Quartz design in an open configuration

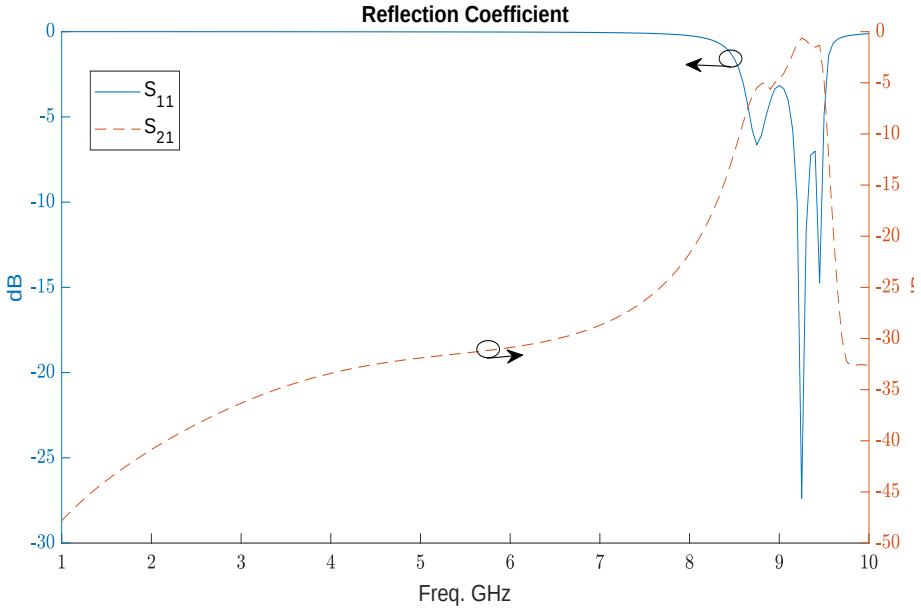

Fig. 6.11: Simulation Results for Si design in an open configuration

CHAPTER 7

Fabrication of Air Spaced and Thick Dielectric MRA

Both MRA designs presented in this thesis were designed to be used as stepping stones toward future MRA compatible technologies TaN and graphene NEMS. For this work to be of value to a future researcher a bill of materials, fabrication, and assembly steps must be provided.

7.1 Parts

7.1.1 Air Spaced MRA

The classic, air spaced MRA, is designed in Chapter 4. This design uses a 'gap' between the two quartz glass substrates. The issue with the design, and main concern, is the brittle nature of glass. In current MRA designs, printed circuit boards (PCBs) are used with mounting holes to provide a way to anchor one substrates to another [19]. With quartz glass, or fused silica, mounting holes need to be milled with special equipment and by special processes. To this end a manufacturer capable of milling and boring holes in quartz glass was selected.

7.1.2 Manufacturer

A manufacturer that provides RF compatible quartz glass is Swift Glass located in Chemung County, New York. Swift Glass has the ability to bore holes into quartz glass substrate. Mounting holes in the MRA substrates is of interest to this design and future work as well. To obtain the correct glass substrates a dimensional drawing must be provided to the manufacturer.

7.1.3 Dimensions and Drawings

In the Air spaced MRA design it is necessary to have both the parasitic and driven element surface bored with holes. The locations of the holes are designed to not interfere with the material deposition of driven element, pixels, and TaN bias lines. Mechanical drawings, with dimensions and the hole locations are provided in Figures 7.1 & 7.2. Additionally a visualization of each antenna layer and the finished assembled geometry are found in Figures 7.3 & 7.4

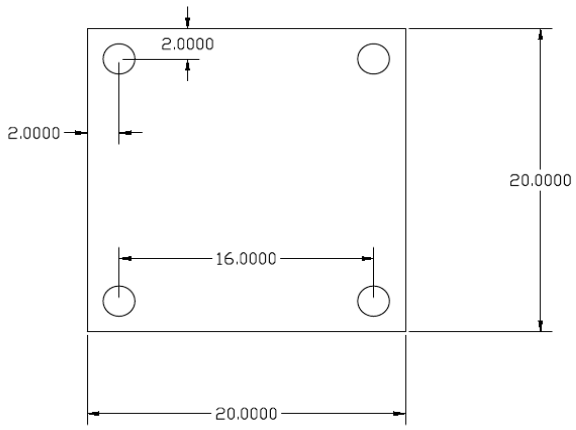

Fig. 7.1: Driven Element substrate layer with dimensions in mm

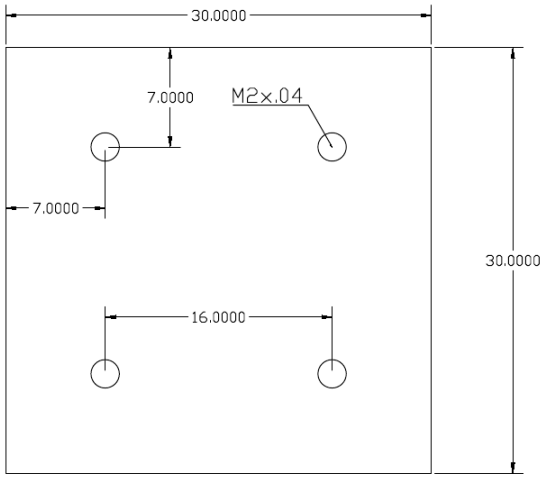

Fig. 7.2: Parasitic substrate layer with dimensions in mm

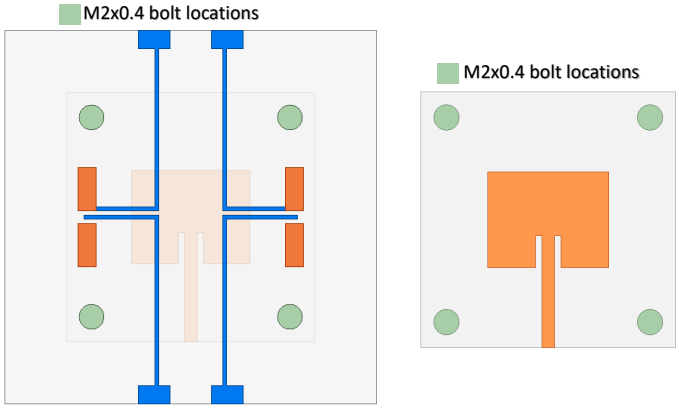

Fig. 7.3: Visualization of the bored holes on a) Parasitic surface, and b) driven element substrate

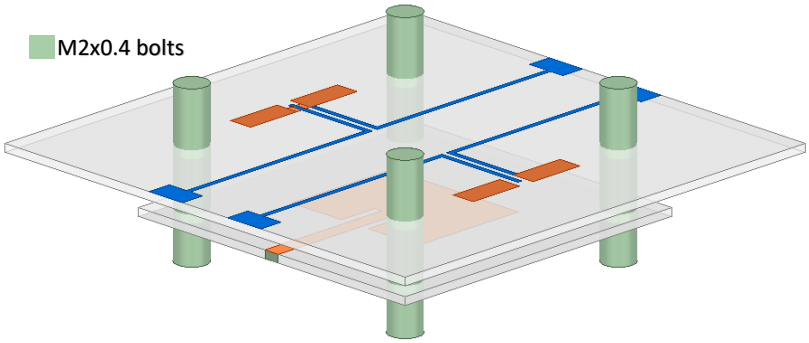

Fig. 7.4: 3-D visualization of the fully assembled Air Spaced MRA with Nylon bolts

7.1.4 Standoffs

Using the bored hole substrates from Swift Glass it is possible to space the two substrates apart. To this end, Nylon threaded rods and nuts must be obtained. Nylon or polyamide is chosen because of its low dielectric constant and high loss at RF frequencies. This will prevent the nylon structure from interfering with the antenna's operation. The threaded rods are chosen to be at least 6 mm in length. The threaded rod must protrude beyond the glass substrates and then be secured with a nylon nut. It is important to minimize any interaction with the antenna and parasitic surface, hence a M2x04 threaded rod/nut pair was selected.

7.1.5 Thick Dielectric MRA

The thick Dielectric MRA design does not need to have mechanical spacing elements to provide an air gap, however, this design does require a piece of 0.5 mm quartz to be glued to the top the driven antenna substrate, which will, then need to be adhered to the driven element surface.

7.1.6 SMA Connection

For both designs a single sub-miniature rev. A (SMA) style connector is chosen to interface between the RF signal generator or network analyzer and the designed MRAs. The SMA connector was first chosen by identifying the operating frequency, (8-10 GHz), then by impedance. The SMA connector must be impedance matched to the transmission line of the antenna. This and the RF generator source are both designed at 50 Ω.

The SMA connector must also be compatible with the physical width of the transmission line feed to the antenna body. Additional care must be taken due to the overhanging quartz substrate design. This addressed by choosing the proper SMA connector. In this design an SMA connector from Amphenol RF, with part number 132415 is chosen [20]. The operating frequency, port impedance, and physical dimensions all match each of the antennas designed ,including the spacing requirements of the Air Spaced MRA. The SMA connector then can be soldered to the antenna feed using indium solder [21] or by using conductive silver epoxies [22].

7.2 Fabrication and Assembly

Using the materials listed in the Bill of Materials (BOM): Appendix A, the MRAs in this thesis can then be fabricated. The fabrication process utilizes a set of masks designed around the antenna element and pixel element geometries. Using these masks metal can be thermally deposited to the quartz substrate then patterned by photolithography. The underside of the driven element layer needs to have a layer of copper or metal deposited for the ground plane.

Following the antenna and pixel element fabrication the SMA connector can then at-

tached to the transmission line of the antenna. This can be done by either indium solder or conductive epoxies [21].

7.2.1 Assembly

Both the air spaced MRA and thick dielectric MRA are assembly methods are discussed below. The Air Spaced MRA is assembled using nylon nuts and bolts. The Dielectric MRA is assembled with glue.

7.2.2 Air Spaced MRA

The nylon bolts fed through each quartz surface with nuts securing the top and underside of each layer. The nuts underneath the parasitic quartz substrate can be adjusted to achieve spacing recommend in the design values.

7.2.3 Thick Dielectric MRA

The thick dielectric MRA is far simpler to fabricate. Once the metal deposition has occurred, the parasitic quartz surface needs to be glued to the antenna layer. This can be done by using Loctite glass glue or epoxies. Loctite glass glue is preferred because it is readily available and has proven in commercial applications [1].

In the Dielectric MRA design care must be taken that glue should be non-interfering with the antenna structure or conductors. In Figure 7.5 areas where adhesives can be applied so the glue is less likely affect the antenna performance is indicated.

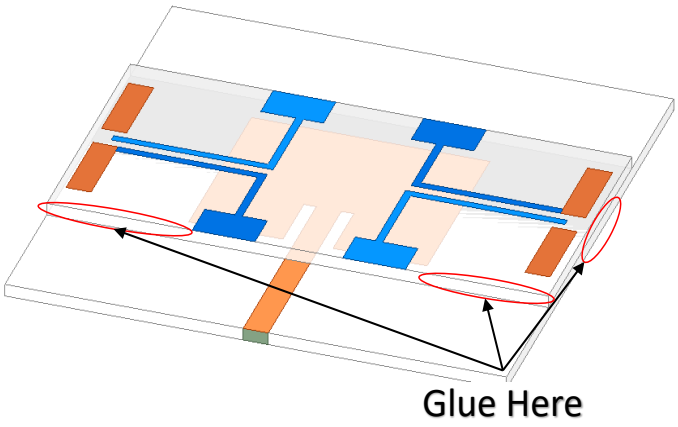

Fig. 7.5**:** Locations where glue can be applied to Dielectric MRA substrate mating surfaces with loctite glass glue [1]

CHAPTER 8

Additional and Future Works

8.1 NEMS

Next steps and future use of the MRA designs presented in earlier chapters using graphene NEMS layouts are conceptualized along side of structures designed to interface between the graphene NEMS switches and a high-frequency RF probe station. This thesis has outlined foundational steps toward the integration and test of graphene-based NEMs structures on MRA parasitic surfaces. This chapter briefly discusses the basic NEMS device structure and layout proposed for future development.

8.1.1 Layout Conceptualization

An early, but flawed, graphene NEMs switch was presented by P. Sharma *et al.* [6]. In Sharma's work the graphene NEMS switch suffers from stiction that leads to the gradual decay of the switching element and eventual device failure. Though there are many ways to counter stiction in NEMS design, two main methods are proposed in future works at USU and NDL; capacitive coupling, and the use of a 'non-stick' surfaces made of carbon nano-tubes (CNT). A conceptual structure of a possible solution is outlined in Figure 8.1.

Though Figure 8.1 shows only the CNT surface NEMS concept, the device can also

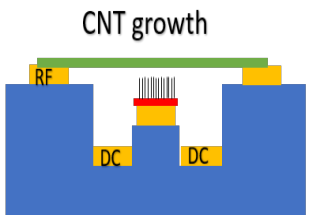

Fig. 8.1**:** Graphene NEMS Concept with CNT Surface

be made without the presence of CNT nonstick layer. Along with the side view presented in Figure 8.1 a simple MRA parasitic surface is also conceptualized in Figure 8.2.

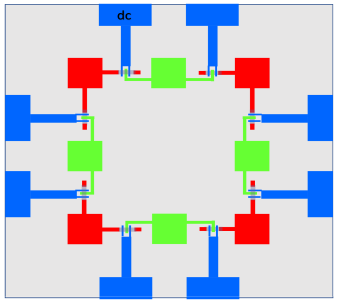

Fig. 8.2**:** Top View of MRA Parasitic with Gr. NEMS

8.1.2 Graphene Growth

The current limitation of this thesis is the ability to obtain and fabricate with graphene material readily. Recently Dr. T.C. Shen and J. Perkins setup a graphene growth system at USU's NDL, however, this needs to be debugged and optimized for single layer graphene growth. Key challenges with the growth of graphene, using available resources, still exist. Before a sample of a graphene NEMS switch can be made, graphene must first be fabricated then patterned by on-campus facilities.

8.1.3 Device Fabrication

Once graphene growth has been fully established, the prototyping of graphene-based NEMS devices can begin. A simplified process for the fabrication of a single element NEMS switch is presented in Figure 8.3. The process utilizes a set of masks that still need to be designed and fabricated.

8.2 Conclusion

Using the work in this thesis and previous work on graphene growth it is possible to fabricate a graphene NEMS switch. The designed MRA structures have shown compatibility with TaN bias lines, and are ready for additional study of graphene nano-structures.

Additionally, a CPW to micro-strip transition is designed for graphene interconnects and graphene NEMS switch characterization.

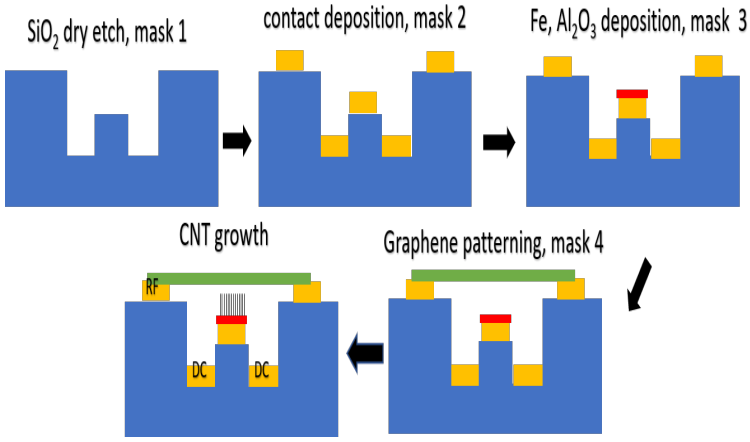

Fig. 8.3: Graphene NEMS Fabrication Process

REFERENCES

[1] *Technical Data Sheet: Loctite Glass Glue*, Henkel, 4 2018.

[2] M. A. Towfiq, I. Bahceci, S. Blanch, J. Romeu, L. Jofre, and B. A. Cetiner, "A reconfigurable antenna with beam steering and beamwidth variability for wireless communications," *IEEE Transactions on Antennas and Propagation*, pp. 1–1, 2018.

[3] Y. Yashchyshyn, "Reconfigurable antennas by rf switches technology," in *2009 5th International Conference on Perspective Technologies and Methods in MEMS Design*, April 2009, pp. 155–157.

[4] S. M. Kim, E. B. Song, S. Lee, S. Seo, D. H. Seo, Y. Hwang, R. Candler, and K. L. Wang, "Suspended few-layer graphene beam electromechanical switch with abrupt on-off characteristics and minimal leakage current," *Applied Physics Letters*, vol. 99, no. 2, p. 023103, 2011. [Online]. Available: https://doi.org/10.1063/1.3610571

[5] C. Lee, X. Wei, J. W. Kysar, and J. Hone, "Measurement of the elastic properties and intrinsic strength of monolayer graphene," *Science*, vol. 321, no. 5887, pp. 385–388, 2008. [Online]. Available: http://science.sciencemag.org/content/321/5887/385

[6] P. Sharma, J. Perruisseau-Carrier, C. Moldovan, and A. M. Ionescu, "Electromagnetic performance of rf nems graphene capacitive switches," *IEEE Transactions on Nanotechnology*, vol. 13, no. 1, pp. 70–79, Jan 2014.

[7] E. Krikorian and R. J. Sneed, "Deposition of tantalum, tantalum oxide, and tantalum nitride with controlled electrical characteristics," *Journal of Applied Physics*, vol. 37, no. 10, pp. 3674–3681, 1966. [Online]. Available: https://doi.org/10.1063/1.1707903

[8] H. Nie, S. Xu, S. Wang, L. You, Z. Yang, C. Ong, J. Li, and T. Liew, "Structural and electrical properties of tantalum nitride thin films fabricated by using reactive radio-frequency magnetron sputtering," *Applied Physics A*, vol. 73, no. 2, pp. 229–236, Aug 2001. [Online]. Available: https://doi.org/10.1007/s003390000691

[9] A. Persano, A. Cola, G. De Angelis, A. Taurino, P. Siciliano, and F. Quaranta, "Capacitive rf mems switches with tantalum-based materials," *Journal of Microelectromechanical Systems*, vol. 20, no. 2, pp. 365–370, April 2011.

[10] P. Sharma, J. Perruisseau-Carrier, C. Moldovan, and A. M. Ionescu, "Electromagnetic performance of rf nems graphene capacitive switches," *IEEE Transactions on Nanotechnology*, vol. 13, no. 1, pp. 70–79, Jan 2014.

[11] C. Mattevi, H. Kim, and M. Chhowalla, "A review of chemical vapour deposition of graphene on copper," *J. Mater. Chem.*, vol. 21, pp. 3324–3334, 2011. [Online]. Available: http://dx.doi.org/10.1039/C0JM02126A

[12] S. A. Campbell and S. A. Campbell, *Fabrication engineering at the micro and nanoscale*. Oxford University Press, 2013.

[13] C. A. Balanis, *Antenna theory: Analysis and design.* John Wiley & Sons, Inc., 2005.

[14] M. A. Matin and A. I. Sayeed, "A design rule for inset-fed rectangular microstrip patch antenna," *WSEAS Transactions on Communications*, vol. 9, no. 1, p. 6372, Jan 2010.

[15] T.-C. Shen, "Tantalum nitride," Apr. 2019, Private Communication.

[16] T. Duong, "ACP-40 GSG250," Feb. 2019, Private Communication.

[17] D. M. Pozar, *Microwave engineering.* Wiley India, 2017.

[18] S. Roddaro, P. Pingue, V. Piazza, V. Pellegrini, and F. Beltram, "The optical visibility of graphene: interference colors of ultrathin graphite on sio2," *Nano Letters*, vol. 7, no. 9, pp. 2707–2710, 2007, pMID: 17665963. [Online]. Available: https://doi.org/10.1021/nl071158l

[19] H.-P. Chang, J. Qian, B. A. Cetiner, F. De Flaviis, M. Bachman, and G. P. Li, "Rf mems switches fabricated on microwave-laminate printed circuit boards," *IEEE Electron Device Letters*, vol. 24, no. 4, pp. 227–229, April 2003.

[20] "Sma end launch recept jack for .032" pcb — 132415." [Online]. Available: https://www.amphenolrf.com/132415.html

[21] R. B. Belser, "A technique of soldering to thin metal films," *Review of Scientific Instruments*, vol. 25, no. 2, pp. 180–183, 1954. [Online]. Available: https://doi.org/10.1063/1.1771017

[22] *8331S Technical Data Sheet*, MG Chemicals, 8 2018, ver 2.10.

APPENDICES

APPENDIX A

Bill of Materials

Item	Source	Specification	Drawing	Quantity	Price
Quartz Glass	Swiftglass	0.5x20x20 mm	Not needed	20	$55.00 ea.
Loctite Glass Glue	Amazon			3	
SMA Connector	Amphenol RF	Part# 132415B		10	$7.82 ea
Epoxy	Amazon	Conductive		1	$53.00 ea.

Table A.1: Bill of Materials for 10 Dielectric MRA

Item	Source	Specification	Drawing	Quantity	Price
Quartz Glass	Swiftglass	0.5x20x20 mm	B.1	10	$65.00 ea.
Quartz Glass	Swiftglass	0.5x40x20 mm	B.2	10	$65.00 ea.
SMA Connector	Amphenol RF	Part# 132415B		10	$7.82 ea.
Nylon bolts	Amazon	M2 x 0.4		1	$7.42
Nylon nuts	DigiKey	M2 x 0.4		80	$0.11 ea.
Epoxy	Amazon	Conductive		1	$53.00 ea.

Table A.2: Bill of Materials for 10 Air Spaced MRA

APPENDIX B

Manufacturer Drawings for Spaced MRA

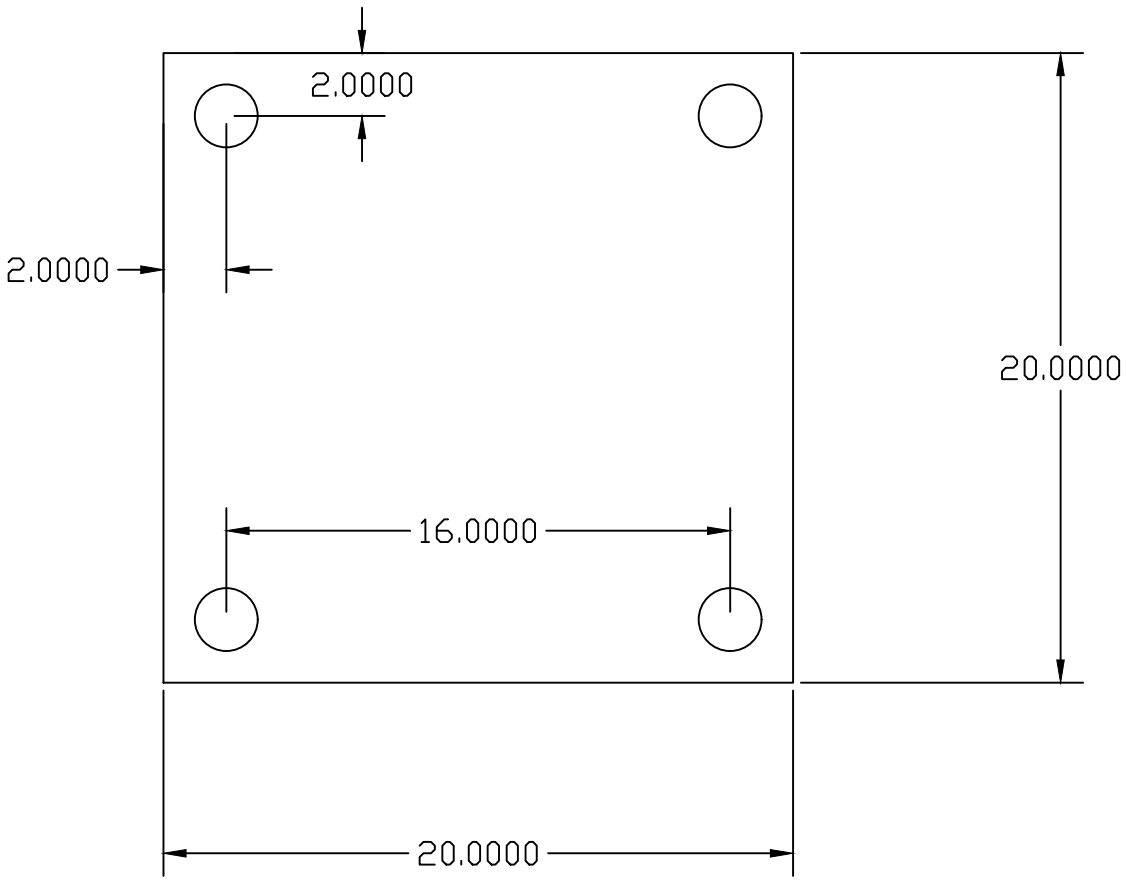

Fig. B.1: Driven element quartz surface drawing with dimensions in mm

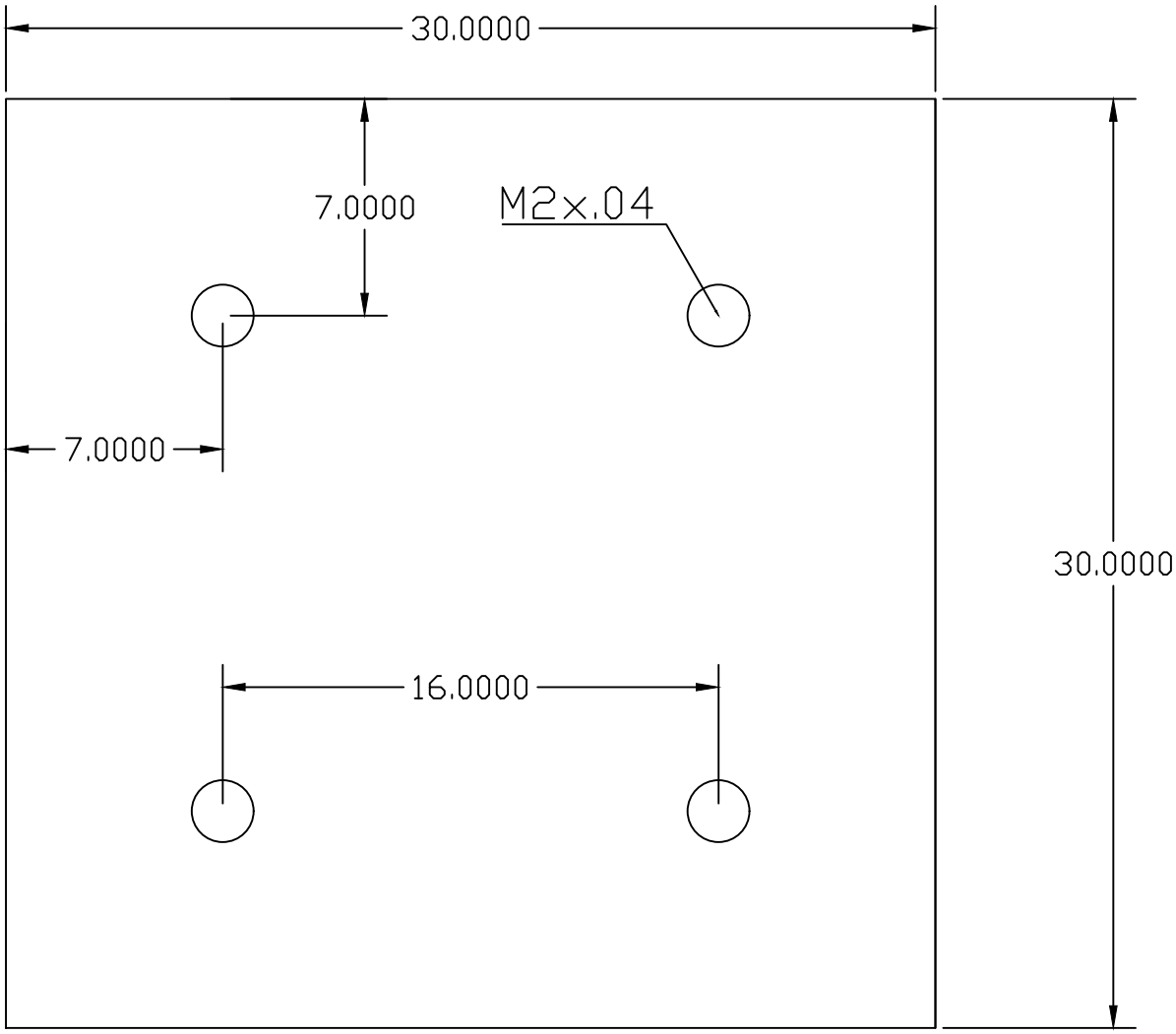

Fig. B.2**:** Parasitic quartz surface drawing with dimensions in mm